

Bifurcations and dynamo action in a Taylor–Green flow

B Dubrulle^{1,3}, P Blaineau¹, O Mafra Lopes¹, F Daviaud¹,
J-P Laval² and R Dolganov²

¹ Groupe Instabilités et Turbulence, SPEC/DRECAM/DSM/CEA Saclay
and CNRS, URA 2464, F-91191 Gif sur Yvette Cedex, France

² Laboratoire de Mécanique de Lille, CNRS, UMR 8107, Blv Paul Langevin,
F-59655 Villeneuve d'Ascq Cedex, France
E-mail: berengere.dubrulle@cea.fr

New Journal of Physics **9** (2007) 308

Received 24 January 2007

Published 31 August 2007

Online at <http://www.njp.org/>

doi:10.1088/1367-2630/9/8/308

Abstract. We report successive bifurcations in direct numerical simulations (DNSs) of a Taylor–Green flow, in both a hydro- and a magneto-hydrodynamic case. Hydrodynamic bifurcations occur in between different metastable states with different dynamo action, and are triggered by the numerical noise. The various states encountered range from stationary to chaotic or turbulent through possible oscillatory states. The corresponding sequence of bifurcations is reminiscent of the sequence obtained in the von Karman (VK) flow, at aspect ratio $\Gamma = 2$ (Nore *et al* 2003 *J. Fluid Mech.* **477** 51). We then use kinematic simulations to compute the dynamo thresholds of the different metastable states. A more detailed study of the turbulent state reveals the existence of two windows of dynamo action. Stochastic numerical simulations are then used to mimic the influence of turbulence on the dynamo threshold of the turbulent state. We show that the dynamo threshold is increased (respectively decreased) by the presence of large scale (resp. small scale) turbulent velocity fluctuations. Finally, DNSs of the magneto-hydrodynamic equations are used to explore the linear and nonlinear stage of the dynamo instability. In the linear stage, we show that the magnetic field favours the bifurcation from the basic state directly towards the turbulent or chaotic stable state. The magnetic field can also temporarily stabilize a metastable state, resulting in cycles of dynamo action, with different

³ Author to whom any correspondence should be addressed.

Lyapunov exponents. The critical magnetic Reynolds number for dynamo action is found to increase strongly with the Reynolds number. Finally, we provide a preliminary study of the saturation regime above the dynamo threshold. At large magnetic Prandtl number, we have observed two main types of saturations, in agreement with an analytical prediction of Leprovost and Dubrulle (2005 *Eur. Phys. J. B* **44** 395): (i) intermittent dynamo, with vanishing most probable value of the magnetic energy; (ii) dynamo with non vanishing mean value of the magnetic energy. We describe a sequence of bifurcation of the dynamo at low Reynolds number and at increasing magnetic Prandtl number, where the dynamo switches from stationary mode to chaotic modes in a complex manner, involving intermittency in a way reminiscent to what is observed in dynamical systems with low number of degrees of freedom.

Contents

1. Introduction	2
2. Results without a magnetic field	3
2.1. Earlier analytic and numerical results about stability	3
2.2. Description of the simulations and their parameter	4
2.3. Successive temporal transitions	4
2.4. Comparison with sequences of bifurcations in VK flow	7
2.5. Convergence towards the mean flow	8
3. Results with a magnetic field	11
3.1. Equations and definitions	11
3.2. Analytical results	12
3.3. Kinematic dynamos	14
3.4. Convergence of Lyapunov exponent	17
3.5. Stochastic-kinematic dynamos	19
3.6. Full coupled problem	26
4. Discussion	35
Acknowledgments	37
References	37

1. Introduction

The Taylor–Green (TG) flow results from a forcing with the two-dimensional (2D) space periodic force proportional to the TG vortex $\mathbf{v}^{\text{TG}} = (\sin x \cos y \cos z, -\cos x \sin y \cos z, 0)$. Despite its simple structure, only few analytical results are presently available regarding its stability properties, or its capability of dynamo action. However, its somewhat special symmetry allows for substantial reduction of the computation work [1], allowing hydro or magneto-hydrodynamic (MHD) simulations at large kinetic or magnetic Reynolds numbers. In the past, it has therefore often been used to explore challenging issues such as singularities in Euler equations [1] or dynamo action at small magnetic Prandtl number [2]–[5].

Another interesting property of the TG flow is its similarity with the von Karman (VK) flow, obtained between two-counter rotating disks. This experimental configuration is used

within the von Karman Sodium (VKS) experiment [6]–[10] to study the dynamo onset and magneto hydrodynamic turbulence in a high Reynolds number unconstrained flow. We therefore used the TG flow as a prototype to understand the mechanism of dynamo onset and dynamo saturation, for use in the analysis of the VKS experimental results. In this process, we obtained several results in the hydrodynamic or magneto-hydrodynamic regime, as side consequences of our exploration of issues related to the dynamo onset. We also report an aspect of the TG flow, we discovered while running MHD simulations: a complex parameter space at low Reynolds number, with coexistence of several metastable states, resulting in possibly non-trivial transition to turbulence or dynamo action. This feature explains several intriguing aspects of dynamo action that had been observed in previous simulations of TG vortex, but never published [11].

The plan of the paper is as follows: in the first part, we set the magnetic field to zero and explore the parameter space of the TG flow as a function of the Reynolds number in the hydrodynamical case. We identify several branches of solution and the bifurcations between them. We sketch the similarity between the sequence of bifurcations we obtain and the successive bifurcations observed in the VK flow. We finally study the convergence from the turbulent state towards the mean flow. In the second part, we also integrate the magnetic field equations and study various aspects connected with dynamo action. After recalling the main equations and definitions, we recall a few analytical results regarding the stability of the TG flow in the MHD case. We then compute the kinematic dynamo thresholds for the different metastable states observed in the hydrodynamic limit. We study the influence of the noise on the dynamo threshold of the turbulent state, in a kinematic limit where there is no back reaction of the magnetic field on the flow. In the last part, we turn to full dynamic simulations of the MHD-TG flow. In the linear stage, we identify interesting dynamo cycles in between metastable states, and show that the magnetic field can favour direct transition from the basic state to the turbulent state. We compute the dynamic dynamo threshold as a function of the Reynolds number. Finally, we explore the possible saturation states of the dynamo and describe an interesting sequence of bifurcations of dynamo states when increasing the magnetic Prandtl number. A discussion of our results in connection to the VKS experiment is finally presented.

2. Results without a magnetic field

2.1. Earlier analytic and numerical results about stability

The TG flow is characterized by the presence of both hyperbolic and elliptic stagnation points. The shortwave asymptotic developed by Lifschitz [12, 13] shows that both types of stagnation points are unstable with respect to shortwave instabilities, no matter which type of flow surrounds them. These instabilities have been studied in the planar TG vortex (with velocity $(\sin x \cos y, -\cos x \sin y, 0)$), by Sipp and Jacquin for the elliptical case [14] and Leblanc and Godeferd [15] for the hyperbolic case. They showed that the elliptic instability deforms the core of the vortices, while the hyperbolic instability favours the formation of longitudinal vortices (the so-called rib). In an earlier numerical study of the TG cell, Lundgren and Mansour [16] derived neutral stability curves and explored the transition to turbulence. They obtained a critical Reynolds number of the order of 10 (respectively 30) for odd (resp. even) modes at low wavenumber (between $2/3$ and 1). The transition to turbulence occurs via the hyperbolic

instability (with counter-rotating swirls perpendicular to the axis), developing into secondary instabilities leading to a turbulent state made of thin elongated vortex tubes and weaker vortex layers which spiral around them.

2.2. Description of the simulations and their parameter

The Navier–Stokes (NS) equations for incompressible fluids are:

$$\partial_t \mathbf{u} + \mathbf{u} \cdot \nabla \mathbf{u} = -\nabla P + \nu \nabla^2 \mathbf{u} + f(t) \mathbf{v}^{\text{TG}}. \quad (1)$$

Here, \mathbf{u} is the velocity, P the pressure, ν the viscosity and $\mathbf{v}^{\text{TG}} = (\sin x \cos y \cos z, -\cos x \sin y \cos z, 0)$ is the TG vortex and $f(t)$ is set by the condition that the modes that correspond to \mathbf{v}^{TG} are kept with constant amplitude. The equations are integrated on a triply periodic cubic domain using a pseudo-spectral method. The aliasing is removed by setting the solution of the 1/3 largest modes to zero. The time marching is done using a second-order finite difference scheme. An Adams–Bashforth scheme is used for the non-linear terms while the dissipative terms are integrated exactly [17]. The control parameter is the Reynolds number $Re = V_{\text{rms}} L_{\text{int}} / \nu$, where $V_{\text{rms}} = \sqrt{2E/3}$ is the rms velocity based on the total kinetic energy $E = \int E(k) dk$ and $L_{\text{int}} = (3\pi/4) \int E(k)/k dk / E$ is the integral scale of the turbulent flow. Both V_{rms} and L_{int} fluctuates with time. Thus, viscosity is dynamically monitored so as to keep Re constant. We have checked that Re is a simple linear function of a geometric Reynolds number (usually used in experiments) based on maximum velocity and half the simulation box $Re = 7.41 V_{\text{max}} \pi / \nu$. Detailed comparison with the previous results obtained by Nore or Ponty can be obtained by multiplying our Reynolds number by a factor $8/\sqrt{3}$, due to our slightly different definition of V_{rms} and L_{int} .

The instabilities and bifurcations we report are obtained in the range $6 < Re < 100$. Below this range, we detected no hydrodynamic instability. Above this range, the computation needs of the direct numerical simulation (DNS) exceeds our computational resources. For DNS at $Re < 46$, the equations were integrated with 64^3 Fourier modes before desaliasing. This resolution was increased up to 96^3 for $46 \leq Re < 75$ and up to 128^3 for $75 \leq Re \leq 100$. The spectral model [18] was used for large-eddy simulations (LES) at $Re = 500$ on 128^3 Fourier modes.

2.3. Successive temporal transitions

During our simulations, we partially explored the phase space of the TG flow by monitoring the time dependence of V_{rms} . When initializing the flow with the TG vortex (in which $V_{\text{rms}} = 0.28$ and $k = \sqrt{3}$), the typical transition scenario we observed is the following (figure 1): first, a very short (lasting typically one or two eddy turnover (ETO) times) relaxation towards a first state, with a low value of V_{rms} , between 0.33 and 0.4. For $Re < 50$, this basic state (state B) is 2D (with zero vertical velocity, see figure 2(a)), stationary and metastable. Its lifetime depends on the Reynolds number (see figure 3): varying from over 250 ETO times at $Re = 8$ –33 ETO for $Re = 25$, and then 22 for $Re = 46$. At $Re = 50$, this stationary state is not observed anymore, and is replaced by a quasi-oscillatory metastable state (O1) (see figure 4(a)), with lifetime independent of the Reynolds number, of the order of 25 ETO time. Due to the numerical noise, these two metastable states bifurcates towards a second state, with a slightly larger V_{rms} , but very different spatial structure. For $Re < 25$, it is another quasi-bidimensional stationary state (state M), with negligible vertical velocity (figure 2(b)), while it becomes chaotic or turbulent (state T1)

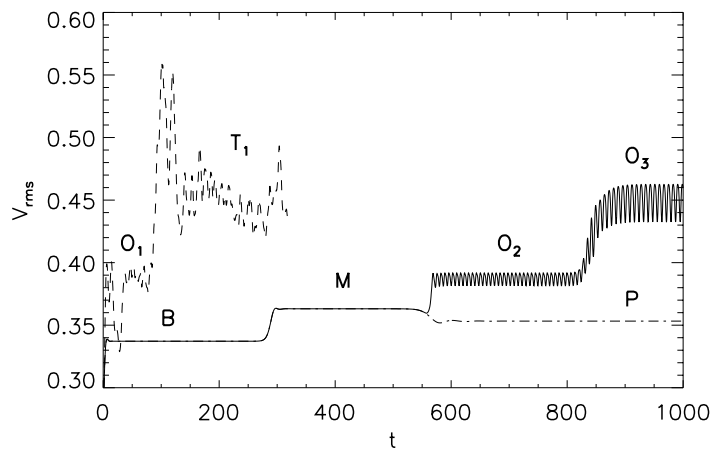


Figure 1. Three typical sequences of bifurcations observed in our TG simulations, with the initial condition given as the TG vortex. Straight line: at $Re = 15$, on a PC computer; dashed-dot line: at $Re = 15$, on IDRIS computer; dashed line: at $Re = 75$, on IDRIS computer. Successive states encountered are labelled (see text for details).

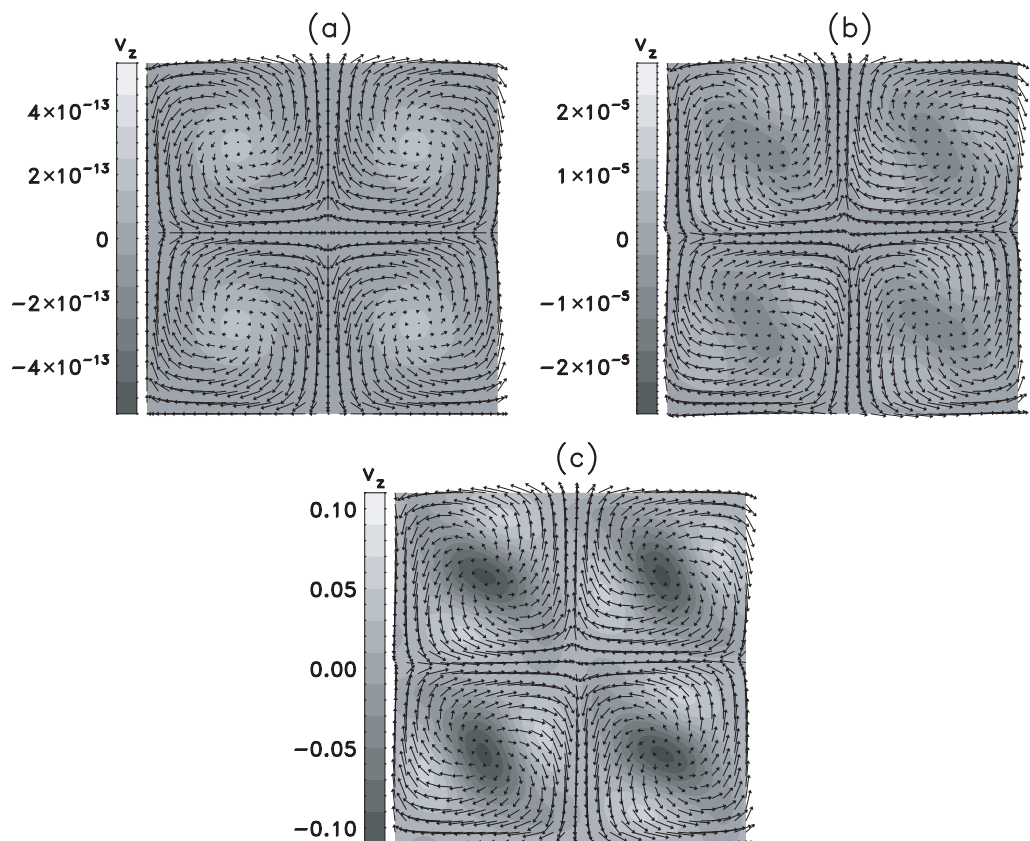


Figure 2. Three stationary states observed in the TG vortex, at $Re = 15$. (a) Basic state B; (b) M state; (c) P state. The plots are horizontal cuts, taken at $z = 0$.

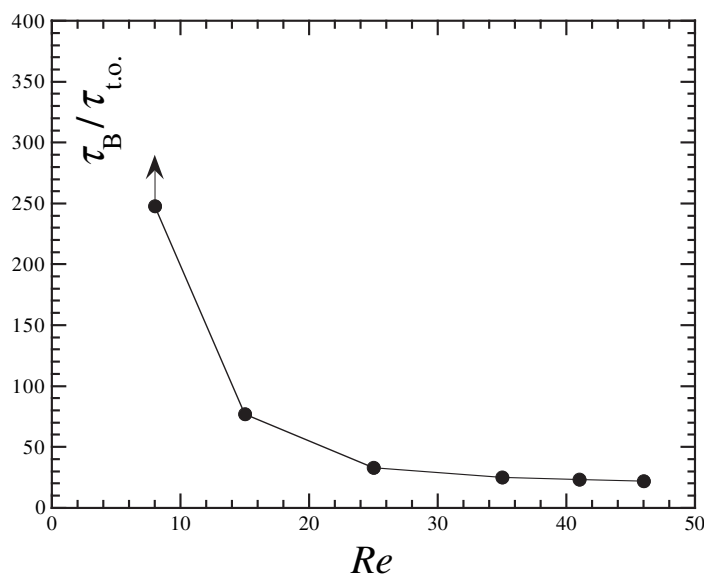


Figure 3. Lifetime of the basic state B, as a function of the Reynolds number. The lifetime is expressed in ETO time. The vertical arrow, at $Re = 8$ indicates that the indicated lifetime is a lower limit. The basic state B becomes unstable between $Re = 40$ and 50 , where it is not observed anymore.

for $Re \geq 25$, with an average spatial structure, see figure 5(a), but no energy in the gravest mode $k = 1$.

The M state observed at low Reynolds number is also metastable, with a lifetime of the order of 50 ETO times. At $Re = 8$ in the presence of additional external noise, we observed a bifurcation towards an oscillatory state, with a period of the order of 50 turnover time. At $Re = 15$, with only the numerical noise, we observed a bifurcation towards a third metastable, stationary state (state P), with nonzero vertical velocity, see figure 2(c). However, when restarting the simulation in the M case, and continuing it on another computer (see figure 1), we obtained instead two successive transitions towards oscillatory states O2 and O3 (see figures 4(b) and (c)). This is an indication that the numerical noise is the engine of the exploration of the phase space and prompted us to introduce external noise to try and induce a bifurcation towards other states (figure 6). We then obtained a bifurcation towards an additional state T2, with a large value of V_{rms} (of the order of 0.4 at $Re = 15$ to 0.51 at $Re = 100$). This state is stable, and oscillatory or quasi periodic until $Re = 8$, and becomes turbulent for a Reynolds number larger than $Re = 8$. An example is provided in figure 6. Looking at the spectra of velocity with and without noise, we noticed that the introduction of noise favours the building of a mode $k = 1$, absent in our initial conditions with $k = \sqrt{3}$ (see figure 7). This mode apparently favours the apparition of a stable, turbulent or chaotic state. It is then tempting to attribute this transition to a short wave instability, identical to the one observed in simulations of the 2D TG vortex (cf previous section), and which should occur above $Re = 10$.

A schematic bifurcation diagram summarizing the various states we encountered in our simulations is drawn in figure 8, using the V_{rms} as order parameter and Re as control parameter.

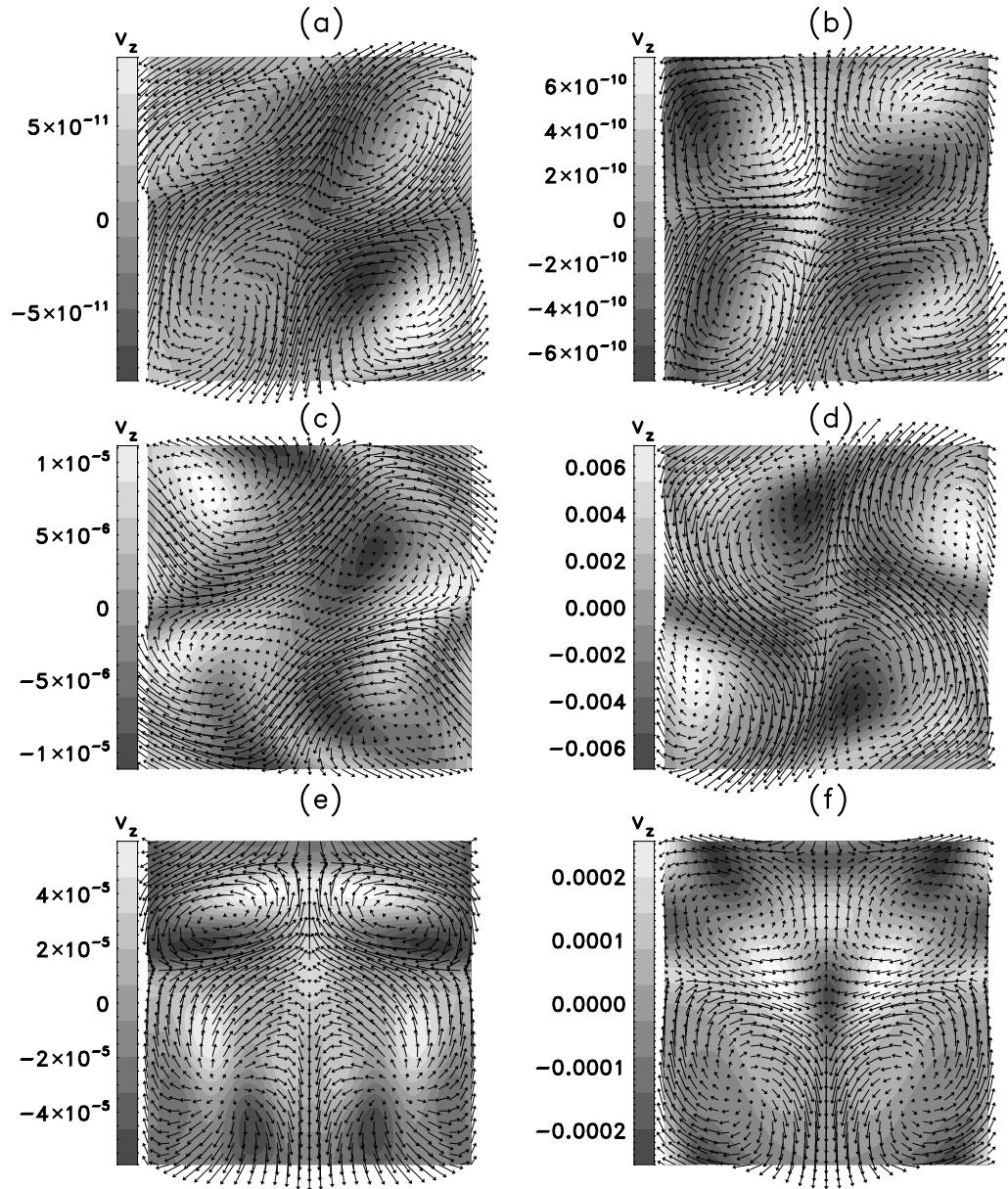


Figure 4. Three oscillatory states observed in the TG vortex: (a) and (b) O1 at $Re = 8$ and at two different times; (c) and (d) O2 at $Re = 15$ and at two different times; (e) and (f) O3 at $Re = 15$ and two different times. The plots are horizontal cuts, taken at $z = 0$. The times are chosen so that high V_{rms} states are on the left and low V_{rms} states are on the right. The flow oscillates in between these two states.

2.4. Comparison with sequences of bifurcations in VK flow

There is a geometric similarity between the TG flow forced at $k = \sqrt{3}$ and the VK flow with aspect ratio $\Gamma = 2$ (so as to obtain square boxes for velocities in a plane) [19]. In both cases, it is a shear layer between two-counter rotating eddies. Boundary conditions, however, are

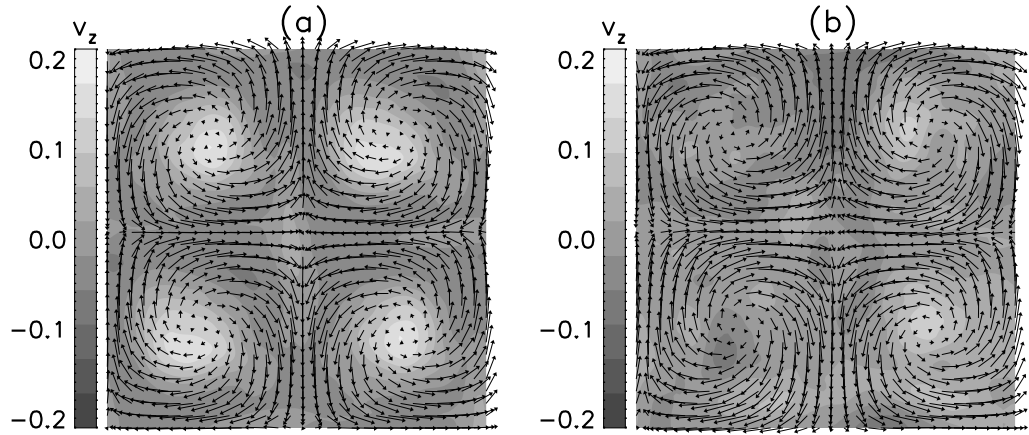


Figure 5. Two time averages of turbulent states observed in the TG vortex at $Re = 100$: (a) with no energy in the mode $k = 1$ (state T1); (b) with energy in the mode $k = 1$ (state T2); the plots are horizontal cuts, taken at $z = 0$.

different: periodic with free-slip (normal component equals zero at the surface) for TG, while the VK flow is enclosed in between two counter rotating disks. Because of the periodicity, and symmetries, the mean helicity in TG is zero, in contrast with nonzero helicity of VK. However, the mean helicity in the box defined by the three planes of mirror symmetry ($x = 0, \pi, y = 0, \pi, z = 0, \pi$) of TG flow is nonzero and its distribution resembles the helicity in VK flow [19]. Similarities between the two flows suggest that the sequence of bifurcations we observe in TG flow could have a counter-part in the VK flow. These sequences of bifurcations have been numerically studied in [20], and experimentally in VK flow driven by smooth disks in [21]. In these publications, the Reynolds number is based on the cylinder radius, and the propeller azimuthal velocity. Taking into account the fact that maximal typical poloidal velocities are of the order of 0.1 the propeller azimuthal velocity, we infer that a conversion factor (division by) of $7.41/0.1 \approx 70$ must be applied to transform their Reynolds number into ours. With this convention, their result can be summarized as follows. Three different steady states with different symmetries are observed: the basic state for $Re < 5$; a mixed mode M with both odd and even harmonics for $5.87 < Re < 6.1$ and a pure mode P ($m = 2$) with only even harmonics for $Re > 6.5$. Travelling waves TW are also observed while increasing the Reynolds number. They originate from a drift pitchfork bifurcation from the mixed mode, occurring at $Re = 6.1$, and give rise to nearly periodic oscillations, with a period of 190 ETO times. When the Reynolds number is increased above $Re = 6.5$, near heteroclinic cycles appear.

This bifurcation diagram bears strong similarity with our diagram. In fact, the portion of our figure between $Re = 6$ and $Re = 15$ looks very similar to the figure 9 of Nore *et al* [20]. Clearly, it would be very interesting to study this analogy in more detail.

2.5. Convergence towards the mean flow

In the course of our work, we came across the problem of computing time-averaged flows, and the question of how long one needs to average a given velocity field to get reliable (time-average independent) results. We thus tried to quantify this effect by defining a global convergence

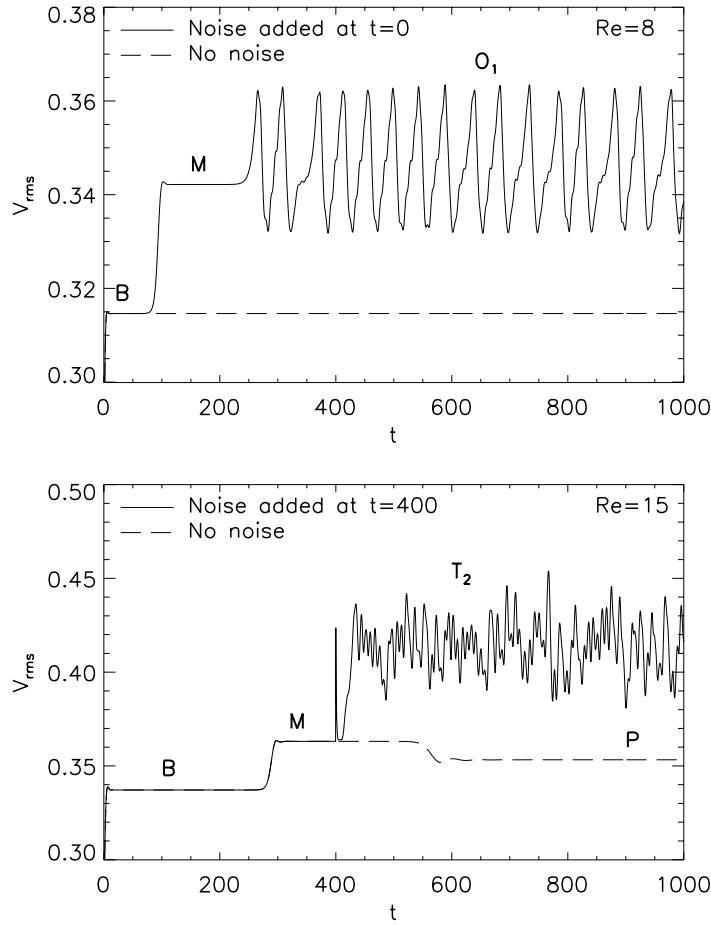


Figure 6. Two typical sequences of bifurcations observed in our TG simulations, with the initial condition given as the TG vortex, and additional external noise allowing population of the mode $k = 1$. Top graph: $Re = 8$, bottom graph: $Re = 15$.

parameter, $\delta(t, T) = \overline{V_{rms}^2}^t / \overline{V_{rms}^2}^T$, where $t < T$. As $t \rightarrow T$, one expects $\delta(t, T)$ to converge towards 1 in an exponential fashion, with a typical time of the order of the correlation time of the slowest structures. Besides, the typical order of magnitude level reached before $\delta(t, T) - 1$ exactly reaches zero is a decreasing function of T . An illustration of this effect is provided in figure 9, for three different Reynolds numbers, $Re = 25, 46$ and 100 , and with T chosen as the longest available time (the simulation duration). In the case $Re = 25$, where a very long integration time has been used (typically 240 ETO times), one sees that the convergence coefficient $\delta(t, T) - 1$ reaches values of the order of 10^{-4} , while, for the larger Reynolds numbers only 125 ETO times were used, the convergence only reaches values of the order of 10^{-3} : the field is ten times less converged. We tried to detect how this convergence occurs, by looking at spectra (figure 10) and velocity field structure (figures 11 and 12). One sees that the effect of averaging is to maintain the constant level of the modes $k = 2$ and $k = 3$, while decreasing the mode $k = 1$ and the modes $k > 3$. In the physical space, the effect is less obvious. In the case $Re = 46$, we had the feeling that averaging leads to a more and more symmetrical

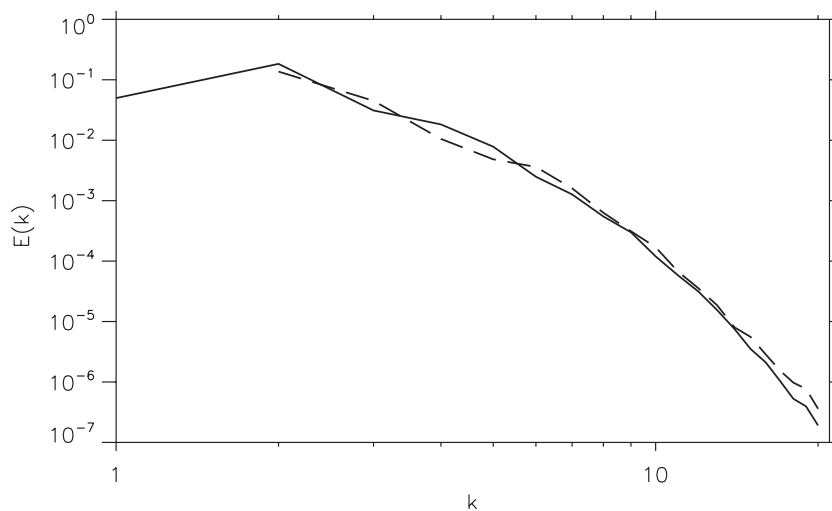


Figure 7. Comparison of the kinetic energy spectrum obtained at a late stage of the simulation, $Re = 25$, with (straight line) and without noise (dashed line).

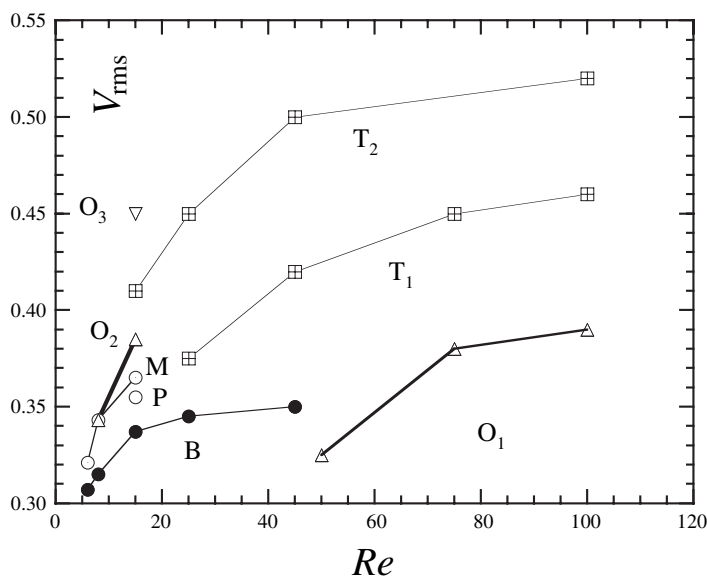


Figure 8. Bifurcation diagram of the TG flow, using V_{rms} as the order parameter and Re as the control parameter. Circles denote stationary states, triangles denote oscillatory states, and squares chaotic or turbulent state. See text for a definition of different states: B, M, P, O1, O2, O3, T1 and T2.

structure, while it tends to decrease and uniformize the vertical component of the velocity in the case $Re = 25$ (making it look more and more like a B or a M state). However, the differences are very small, and all velocity fields look very similar.

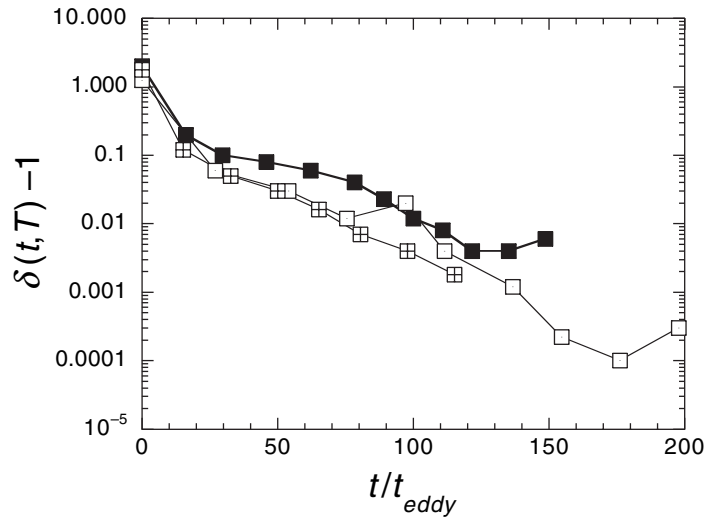


Figure 9. Convergence parameter $\delta(t, T) - 1$ as a function of t/t_{eddy} for different Reynolds numbers: \square $Re = 25$, $T = 200 t_{\text{eddy}}$; \boxtimes $Re = 46$, $T = 125 t_{\text{eddy}}$; \blacksquare $Re = 100$, $T = 150 t_{\text{eddy}}$.

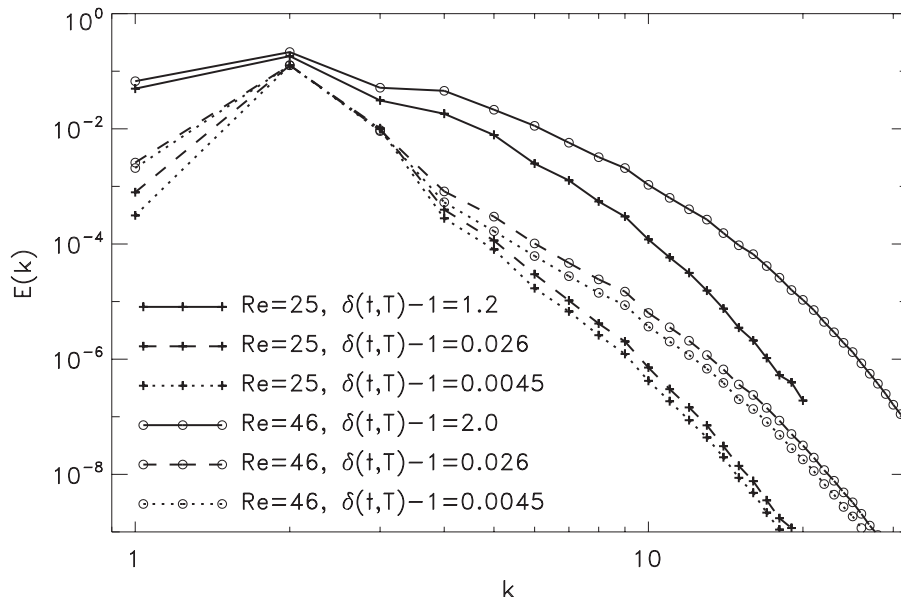


Figure 10. Spectrum of the mean velocity field, as a function of the convergence parameter at $Re = 25$ and 46 .

3. Results with a magnetic field

3.1. Equations and definitions

In the MHD case, the equations of motion are now:

$$\partial_t \mathbf{u} + \mathbf{u} \cdot \nabla \mathbf{u} = -\nabla P + \nu \nabla^2 \mathbf{u} + \mathbf{j} \times \mathbf{B} + f(t) \mathbf{v}^{\text{TG}}, \quad \partial_t \mathbf{B} = \nabla \times (\mathbf{u} \times \mathbf{B}) + \eta \nabla^2 \mathbf{B}. \quad (2)$$

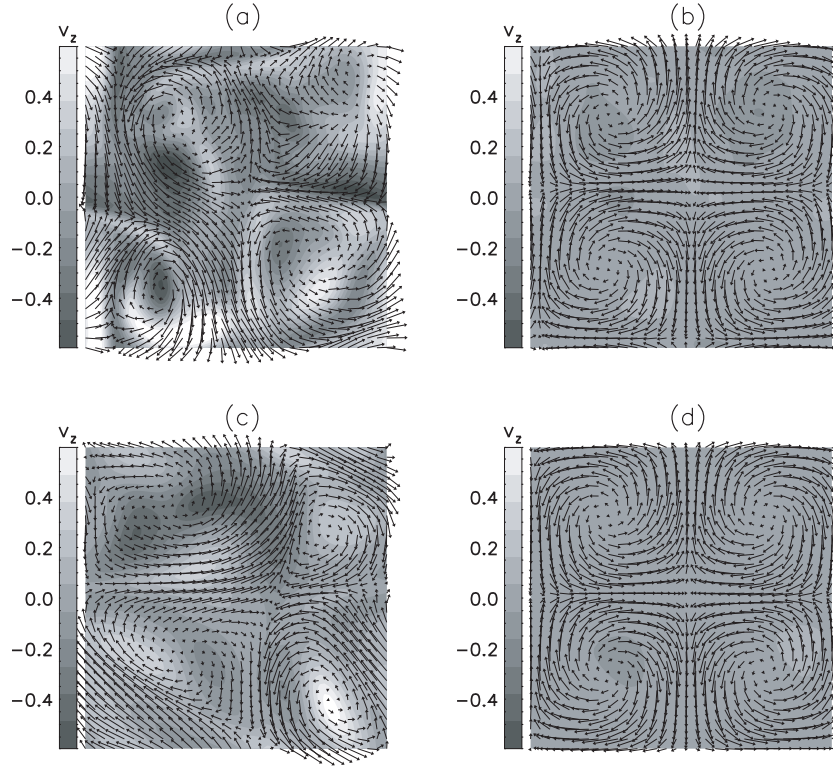


Figure 11. Velocity fields as a function of the convergence. (a) $Re = 46$ instantaneous; (b) $Re = 46$, $\delta = 1.0045$; (c) $Re = 25$ instantaneous; (d) $Re = 25$, $\delta = 1.0045$. The plots are horizontal cuts, at $z = 0$.

In addition to variables already defined in previous sections, the new symbols are now \mathbf{B} the Alfven velocity, η the magnetic diffusivity and $\mathbf{j} = \nabla \times \mathbf{B}$ the current density. The forcing is done like in the hydrodynamical case. Our simulations therefore differ with simulations reported in [3, 4] that are at constant force. The two control parameters are now the Reynolds number Re and the magnetic Reynolds number $Rm = V_{rms} L_{int} / \eta$. Both viscosity and diffusivity are dynamically monitored so as to keep Re and Rm constant. The ratio $Rm / Re = Pm$ is the magnetic Prandtl number.

3.2. Analytical results

There is no systematic analytical study of the TG flow in the MHD case. Partial results regarding the stability of the TG vortex with respect to large scale perturbation have been obtained through multi-scale techniques by Lanotte *et al* [22]). In this mean field type of approach, one finds that the major effect of a given incompressible flow \mathbf{u} on the mean (large scale) magnetic field $\overline{\mathbf{B}}$ is to generate a mean electromotive force $\overline{\mathbf{E}}$ in the mean induction equation, so that:

$$\partial_t \overline{\mathbf{B}} = (\nabla \times \overline{\mathbf{E}}) + \eta \nabla^2 \overline{\mathbf{B}}, \quad \overline{\mathbf{E}} = \alpha_{ij} \overline{B_j} + \beta_{ijk} \partial_j \overline{B_k}, \quad (3)$$

where α_{ij} and β_{ijk} are functions of \mathbf{u} .

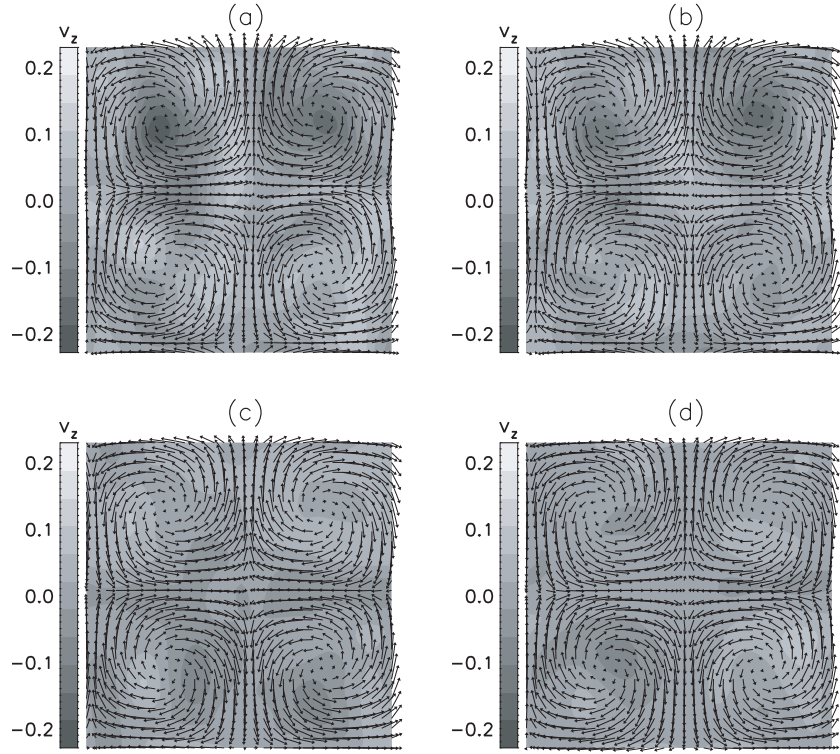


Figure 12. Velocity fields as a function of the convergence: (a) $Re = 46$, $\delta = 1.026$; (b) $Re = 46$, $\delta = 1.0045$; (c) $Re = 25$, $\delta = 1.026$; (d) $Re = 25$, $\delta = 1.0045$. The plots are horizontal cuts, at $z = 0$.

Lanotte *et al* computed the values of α and β for the velocity field:

$$\begin{aligned} u_x &= \sin x \cos y \cos z + A \sin 2x \cos 2z + B(\sin x \cos 3y \cos z + 5/13 \sin 3x \cos y \cos z), \\ u_y &= -\cos x \sin y \cos z + A \sin 2y \cos 2z - B(\cos 3x \sin y \cos z + 5/13 \cos x \sin 3y \cos z), \\ u_z &= -A(\cos 2x + \cos 2y) \sin 2z + B(2/13 \cos x \cos 3y \sin z - 2/13 \cos 3x \cos y \sin z), \end{aligned} \quad (4)$$

where A and B are free parameters. When $A = B = 0$, the velocity field is just the TG vortex, equal to the TG flow in the limit of infinite viscosity. When $A \propto Re$ and $B \propto Re^2$, this velocity field can be seen as the solution of the expansion of the TG vortex to second-order in Re .

Due to the parity invariance of the flow, the α coefficient is zero. The β coefficient however depends on the velocity field: it is always positive for the TG vortex ($A = B = 0$), but can take negative values when A and B are different from zero, for large enough magnetic Reynolds number. This induces a large-scale instability for the magnetic field, for $Rm > 4.4$ for $A = 1$, $B = 0$ or $Rm > 3$ for $A = B = 1$. The most unstable mode lies in the xy -plane, with a corresponding eigen-component of the form $\mathbf{B} = (0, 0, B_z \exp i\mathbf{k} \cdot \mathbf{x})$. This instability corresponds to a dynamo action through negative magnetic eddy diffusivity, and occurs at wavenumbers smaller than the scale of the basic flow.

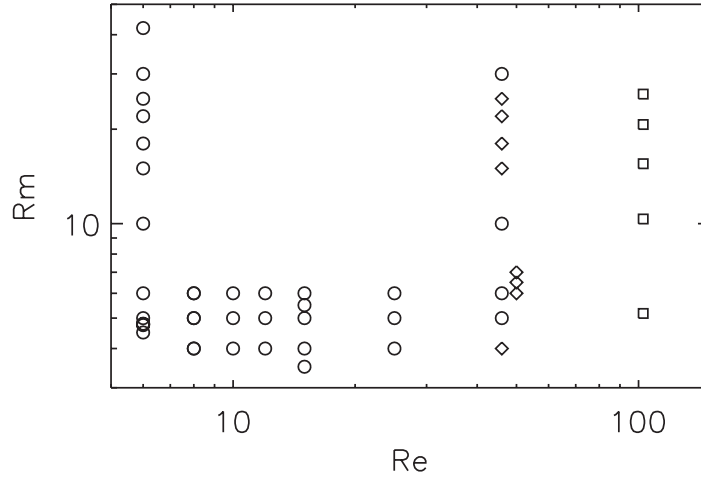


Figure 13. Parameters of the DNS used to define the critical magnetic Reynolds number. The three symbols represent three different spatial resolutions used in the simulations: 64^3 (\circ), 96^3 (\diamond) and 128^3 (\square).

3.3. Kinematic dynamos

3.3.1. General procedure. Kinematic dynamos are obtained by integrating only the induction equation and keeping the velocity field equal to a constant given velocity field (time average of the different stable or metastable states observed in our simulations):

$$\partial_t \mathbf{B} = \nabla \times (\bar{\mathbf{u}}^T \times \mathbf{B}) + \eta \nabla^2 \mathbf{B}, \quad \bar{\mathbf{u}}^T = \frac{1}{T} \int_0^T \mathbf{u}(t) dt, \quad (5)$$

where T is less than the lifetime of the considered state. Kinematic dynamos have been studied for different metastable states observed in our simulations. For this, we proceed in two steps. First, compute a time-averaged velocity field from a time series of a DNS in a given metastable state. Then, plug this (time-independent) velocity field in the induction equation (5) and study the evolution of a given seed magnetic field of given amplitude (with an energy of the order of 10^{-4} of the kinetic energy of the averaged field). For this, we fix Re , vary Rm and monitor the time behaviour of the magnetic energy $\langle B^2 \rangle$ and the finite-time Lyapunov exponent $\Lambda = 0.5 \partial_t \langle \ln(B^2) \rangle$, where the average is taken over the spatial domain. Two types of behaviours are typically observed: (i) no dynamo: the magnetic energy decays, the Lyapunov exponent converges towards a finite negative value (ii) dynamo: the magnetic energy grows exponentially with positive Lyapunov exponent. A critical magnetic Reynolds number for the dynamo threshold is then computed from the values of the Lyapunov exponent in dynamo and no dynamo regimes, via a standard interpolating procedure. A large number of simulations was necessary to define the critical magnetic Reynolds number for each Reynolds number. For compactness, we have listed each simulation in the graph of figure 13. The three symbols represent three different spatial resolutions that were adapted to Re and Rm .

3.3.2. Critical magnetic Reynolds number. We have computed the kinematic critical Reynolds number, as a function of the Reynolds number, for different metastable states. The values we obtained are summarized in table 1 and figure 14. Note that all the mean fields give a critical

Table 1. Critical kinematic magnetic Reynolds numbers for various averaged metastable velocity fields. The type denotes the velocity field from which the average has been obtained. The corresponding V_{rms} has also been indicated. Note that, for non-stationary fields, V_{rms} of the averaged fields is lower than the average of V_{rms} of the instantaneous field.

Re	Rm_c	V_{rms}	Type
6	4.81	0.31	B
6	5.78	0.32	M
8	5.89	0.34	O2
10	5.47	0.30	T2
12	5.37	0.30	T2
15	3.33	0.37	M
15	4.07	0.36	P
15	5.33	0.30	T2
25	4.43	0.33	T1
25	5.59	0.30	T2
46	4.50	0.32	T1
46	6.6	0.30	T2
50	6.13	0.32	O1
100	4.50	0.32	T1
100	6.6	0.30	T2

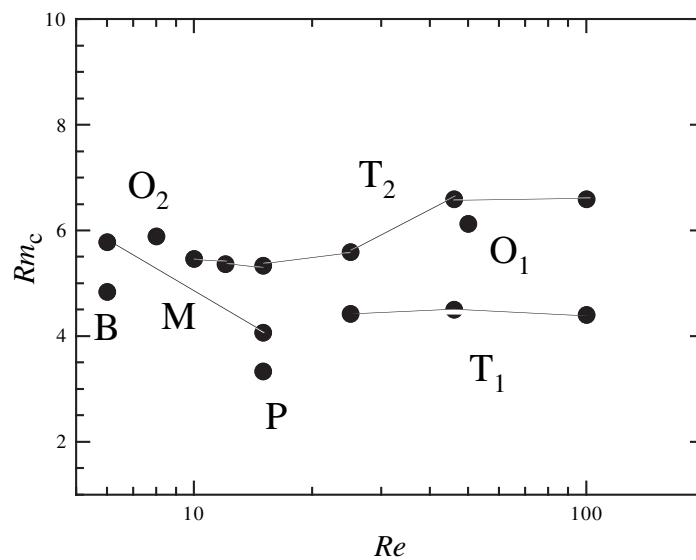


Figure 14. Critical kinematic magnetic Reynolds number, as a function of Re , for various averaged meta-stable states obtained in our simulations. The symbols near the curve denote the state from which the mean field used in the kinematic simulations has been obtained.

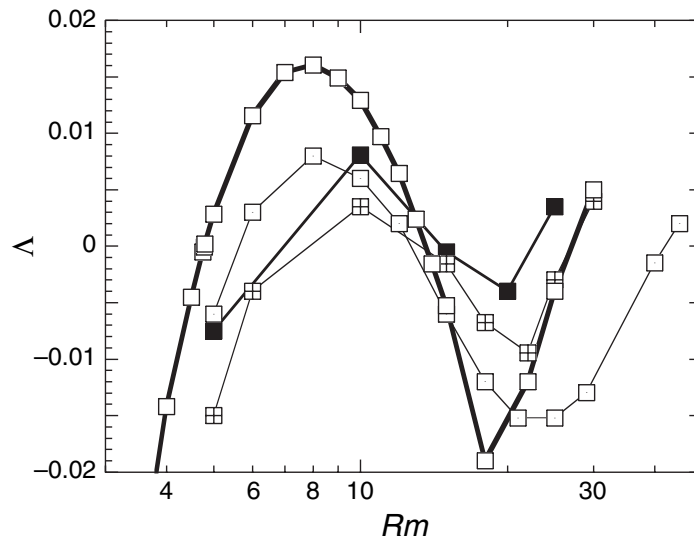


Figure 15. Lyapunov exponents Λ as a function of the magnetic Reynolds number for the turbulent state T2 for kinematic dynamo, at different Reynolds numbers: \square $Re = 6$; $\square \cdot$ $Re = 25$; \boxplus $Re = 46$; \blacksquare $Re = 100$.

magnetic Reynolds number between $Rm_c = 3.3$ and 7. This means that it is less sensitive to the spatial structure of the flow, than in a non-periodic flow, with boundary layers [23, 24]. This could be traced to another mechanism of dynamo action, via stagnation or hyperbolic points (fast dynamo mechanisms), rather than through boundary layers (slow dynamo mechanism).

3.3.3. Dynamo windows. Because of its possible relevance to the analysis of the dynamical dynamos, we have studied the turbulent mean field T2 in greater detail, by computing Lyapunov exponents over a large range of magnetic Reynolds numbers. The result is provided in figure 15, for T2 fields obtained at $Re = 25, 46$ and 100 . For comparison, the Lyapunov exponent for the basic state B at $Re = 6$ is also provided. One sees that the Lyapunov exponents do actually cross the value $\Lambda = 0$ at three locations $Rm_c^{(1)} < Rm_c^{(2)} < Rm_c^{(3)}$, indicating the presence of at least two dynamo windows, illustrated in figure 16 and detailed in table 2. The first dynamo window, occurring around $Rm = 10$ for all Reynolds numbers, corresponds to a stationary mode. The second dynamo window, occurs for decreasing values Rm as Re is increased beyond $Re = 25$. This situation is therefore very similar to the ABC flow with $A = B = C = 1$, where two windows of dynamo action have been reported: one around $Rm = 6$ [25], and one starting at $Rm > 14$ [26]. The latter corresponds to an oscillatory mode until $Rm = 100$, where it is replaced by a stationary mode [27]. Such a mode crossing could occur in the TG flow, a possibility that could be worth exploring. Note that when looking at the Lyapunov exponent as a function of averaging, we indeed detected oscillatory dynamos near the border of the second dynamo window, with oscillations of the magnetic energy over a very long period (between 200 and 500 ETO) (figure 17). If such oscillatory modes are present in the second dynamo window, they may have a very large oscillation period and may prove very difficult to detect. For the time being, neither our group, nor the Boulder group [28] were able to detect any such oscillations in the second dynamo window.

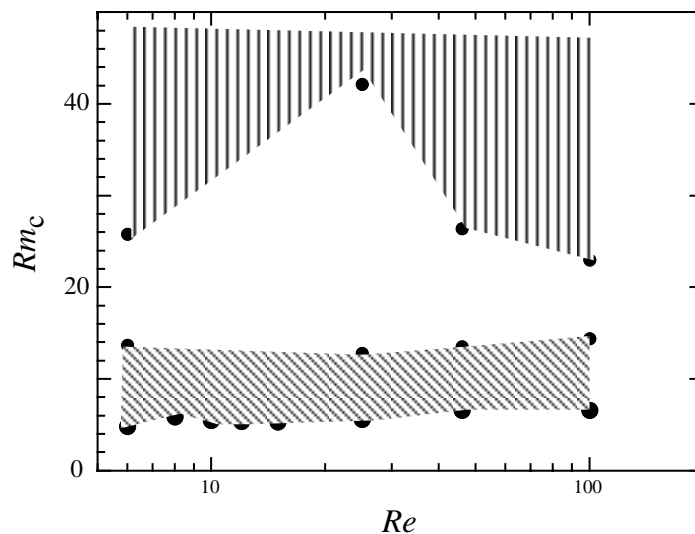


Figure 16. Windows of dynamo action for the turbulent state, as a function of the Reynolds number. The dashed area corresponds to the region of the parameter space where kinematic dynamo is observed, corresponding to positive values of the Lyapunov exponent.

Table 2. Critical magnetic Reynolds numbers for kinematic dynamo action in the state T2, at different Reynolds numbers. $Rm_{c,1}$ and $Rm_{c,2}$ correspond respectively to the beginning and the end of the window of stationary dynamo action, while $Rm_{c,3}$ corresponds to the beginning of the window for oscillatory dynamo action.

Re	$Rm_{c,1}$	$Rm_{c,2}$	$Rm_{c,3}$
6	4.81	13.7	25.8
25	5.53	12.8	42.2
46	6.60	13.5	26.4
100	6.60	14.4	23.0

3.4. Convergence of Lyapunov exponent

To understand the influence of convergence on the dynamo threshold, we have also studied the influence of the averaging on the Lyapunov exponent by performing kinematic simulations with velocity fields averaged over different timescales. In order to allow the removing of many scales through the averaging, we have conducted this study at a rather large Reynolds number $Re = 46$, where the flow is already fully turbulent and quite different from the mean velocity field (see figures 11 and 12). The result is provided in figure 18. Interestingly enough, one sees that the averaging mostly affects the large Rm part of the Lyapunov exponent. For the instantaneous field (no averaging), the decrease of the Lyapunov exponent between $Rm = 10$ and 18 (responsible for the apparition of a second dynamo of dynamo action) is either removed or shifted towards larger Rm (out of reach to simulations). As the averaging process is

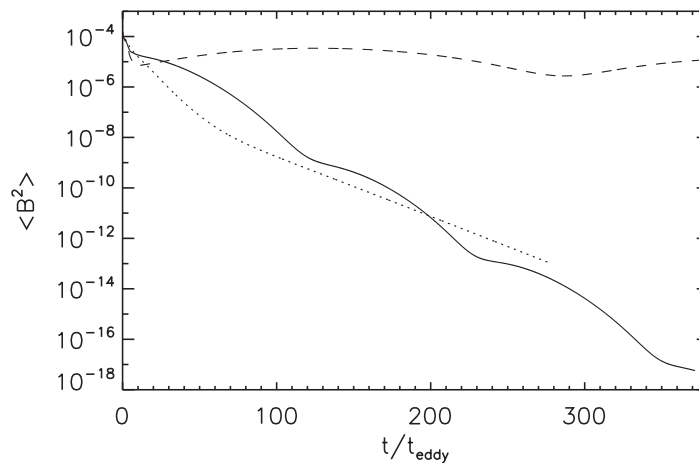


Figure 17. Magnetic energy as a function of time for kinematic simulations at $Re = 46$ and $Rm = 18$ at different averaging period T , displaying oscillations over very long periods: $---$ $T/t_{\text{eddy}} = 33$; $—$ $T/t_{\text{eddy}} = 65$; \cdots $T/t_{\text{eddy}} = 130$.

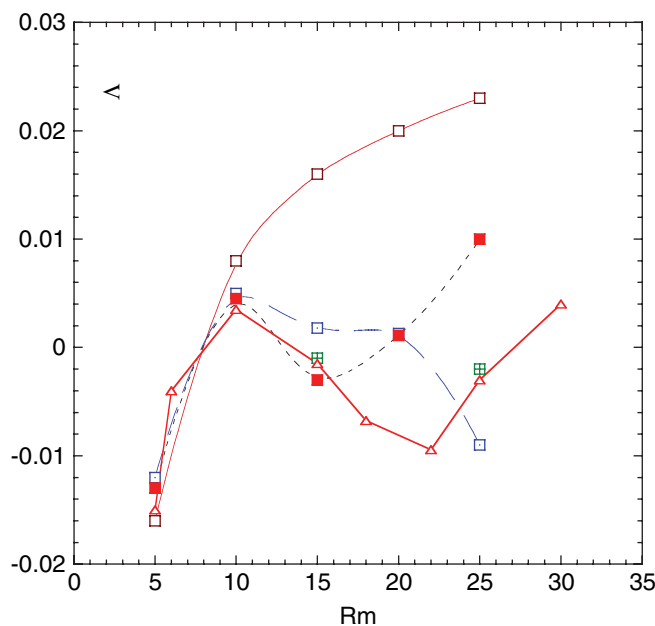


Figure 18. Lyapunov exponent Δ as a function of Rm for a velocity field at $Re = 46$ after different averaging periods T : \square $T/t_{\text{eddy}} = 0$; \square $T/t_{\text{eddy}} = 50$; \boxplus $T/t_{\text{eddy}} = 80$; \blacksquare $T/t_{\text{eddy}} = 113$; \triangle $T/t_{\text{eddy}} = 130$.

operating, the Lyapunov exponent slowly bends downwards, ensuring the apparition of the second dynamo window. Note however that the location of the first dynamo window is not affected by the length of the averaging, so that the kinematic simulations with the frozen velocity field gives a lower critical magnetic Reynolds number than the dynamical velocity field. This seems to contradict a belief in the dynamo community, but we have no obvious explanation for this fact.

3.5. Stochastic-kinematic dynamos

3.5.1. Motivation. Many recent dynamo experiments are based on liquid sodium, characterized by a very low magnetic Prandtl number. At the dynamo threshold, the flow is then necessarily highly turbulent, with a large Reynolds number and large fluctuation level (as high as 50%). From a theoretical point of view, the corresponding dynamo can be regarded as an instability (driven by the mean flow) in the presence of a multiplicative noise (turbulent fluctuations). Based on this remark, Leprovost and Dubrulle [29] derived an analytical prediction regarding the turbulent dynamo using tools borrowed from the study of a noisy Duffing oscillator [30]. They found that noise could favor or impede the magnetic field growth depending on the fluctuation intensity or correlation time. They also found that the transition to a turbulent dynamo (at $Rm = Rm_{ct}$ with a nonzero mean field value) does not occur directly from the trivial, zero-field state, but is preceded by an intermittent regime of the magnetic field, occurring at $Rm = Rm_{ci}$. There is then a whole range of magnetic Reynolds numbers for which the intermittent behaviour is observed: $Rm_{ci} < Rm < Rm_{ct}$. In the isotropic case, Rm_{ci} is a non-monotonic function of the noise intensity: Rm_{ci} is larger than the critical magnetic Reynolds number with no-noise Rm_{c0} at small noise amplitude, while it becomes $Rm_{ci} < Rm_{c0}$ at large noise amplitude. Furthermore, in a numerical study of the noisy Bullard dynamo (a 2D solid dynamo) [31], Rm_{ct} is found to be a monotonic increasing function of noise intensity, so that noise always delays transition towards a turbulent dynamo state. Some of these findings have recently been reproduced experimentally in a Bullard-VK dynamo, where the intermittent regime (often referred to on-off regime) has been observed [32].

However, their simple model ignores the molecular magnetic diffusivity. This motivates new types of simulations—stochastic-kinematic dynamo (KS)—to investigate the validity and limitation of their results, when molecular diffusivity is taken into account. Stochastic-kinematic simulations will also prove useful to interpret the outcome of DNSs within the Kraichnan–Kazantsev model of MHD flows, where turbulence is replaced by a suitable noise.

3.5.2. Notations and definitions. In the kinematic-stochastic case, the velocity field $\mathbf{u} = \bar{\mathbf{u}}(Re) + \mathbf{v}'(k_I, \tau_c)$ is the sum of a time averaged velocity field at a given Re and of an external Markovian Gaussian noise, with fixed amplitude v' , correlation time τ_c and typical scale k_I . The control parameters are therefore Rm , v' , τ_c and k_I . To make an easier connection with the DNSs, where Re is an essential control parameter, we introduce a noise intensity parameter, $\delta \equiv \delta(0, T) = \overline{\langle u^2 \rangle} / \langle \bar{u}^2 \rangle$. This parameter depends on the noise amplitude, as well as its correlation time and characteristic scale, and needs to be computed for each stochastic simulation. It can also be computed in the direct simulations, and is found to depend on the Reynolds number, increasing from a value of 1 at low Reynolds number, until about 3 at the largest Reynolds number (figure 19(a)). Note that $\delta - 1$ is also connected to the difference between the total kinetic energy and the kinetic energy of the mean flow, a quantity which increases with the Reynolds number, see figure 19(b). Another interesting non-dimensional parameter is given by the variation of the instantaneous total kinetic energy (see figure 20). This variation can be quantified by a second parameter $\delta_2 = \sqrt{\langle u^2 \rangle^2 - \langle \bar{u}^2 \rangle^2} / \langle \bar{u}^2 \rangle$. In the sequel, we show that all our results can be interpreted using δ and δ_2 as a control parameter.

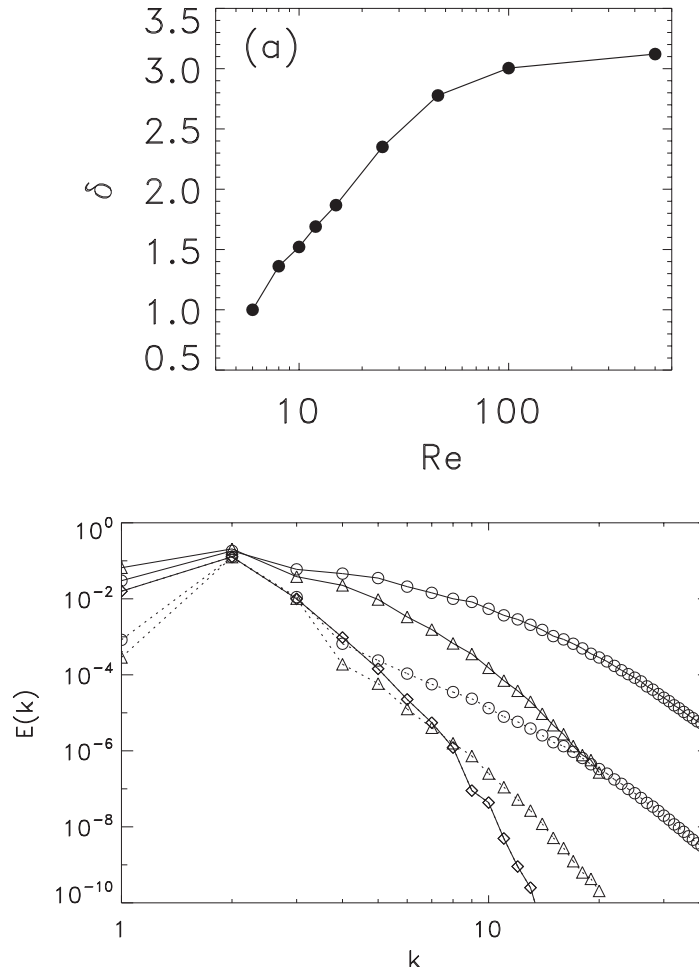


Figure 19. (a) Noise intensity $\delta = \overline{\langle u^2 \rangle} / \langle \bar{u}^2 \rangle$, as a function of the Reynolds number, measured in our DNS and LES simulations under the dynamo threshold. (b) Energy spectrum of the velocity field in the DNS (full line with symbols) and in the mean field (dotted line with symbols), at different Reynolds numbers: $\diamond Re = 6$, $\triangle Re = 46$ and $\circ Re = 100$.

3.5.3. The parameter space. We have considered noise at large ($k_l = 1$) and small scale ($k_l = 16$), with correlation time ranging from 0 to 50 s, i.e. from 0 to 17 ETO time. An example of our noise power-spectrum is provided in figure 21 for different correlation times. It is essentially a white noise (flat spectrum) until $f_0 \sim 1/6\tau_c$, with rapid decrease after f_0 . From now on, we express all values of τ_c in units of the ETO time. The spatial resolutions of stochastic-kinetic simulations are equivalent to the resolutions of the kinetic simulations without noise at the same Reynolds numbers.

Since the kinematic dynamo threshold is essentially constant for all values of the Reynolds number (see $Rm_{c,1}$ on table 2), we first focus on the study of the case where the time-averaged field is fixed as $\bar{u}(Re = 6)$ and vary the noise amplitude, characteristic scale or correlation time, to explore their influence on the dynamo threshold. Our exploration of the parameter space is provided in figure 22, for different kinds of noise and $\bar{u}(Re = 6)$. Note that by using our external

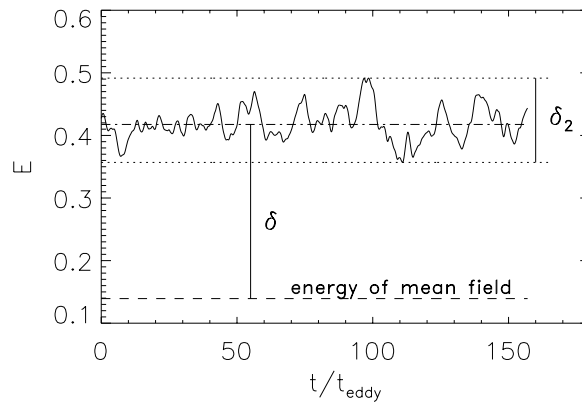


Figure 20. Typical variation of the fluctuation kinetic energy, as a function of time ($Re = 100$): dotted line: for the mean field; full line: for the instantaneous field. The vertical lines indicate that δ quantifies the ratio of mean energy of the total field to the energy of the mean field, while δ_2 quantifies the fluctuations of total kinetic energy over the mean energy of the total field.

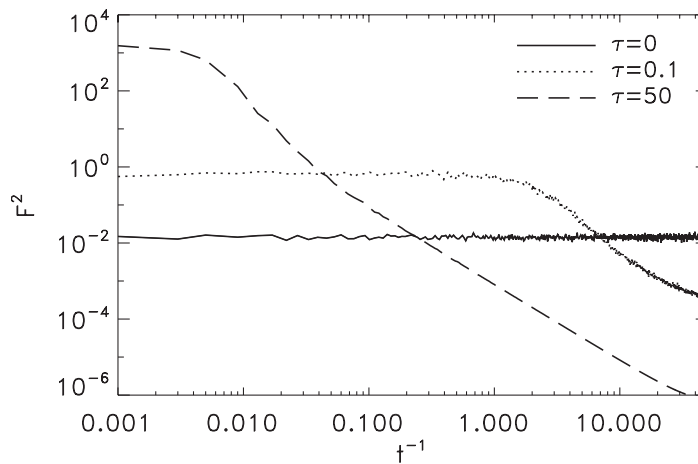


Figure 21. Power spectrum of the noise used in our KS simulations, at different values of τ_c .

noise, we are able to produce noise intensities of the order of the noise intensities measured in experiments ($\delta \sim 10$ at $Re \sim 10^6$ for the VK flow), and that are out of reach of DNS.

3.5.4. Dynamo threshold. For low correlation time or injection scale, we are actually able to follow the deformation of the two windows of dynamo action. One sees that a noise does not destroy them, but rather distorts them. In the case where the noise is at small scale ($k_I = 16$, i.e. at a scale smaller than the dissipative length scale for any $Rm \leq 40$), the two windows are slightly tilted downwards, while they are lifted upwards in the case of large scale noise ($k_I = 1$). The influence of the noise on the first dynamo bifurcation (the dynamo threshold) can be summarized by plotting the critical magnetic Reynolds numbers as a function of the noise intensity (figure 23(a)). Large scale (resp. small-scale) noise tends to increase

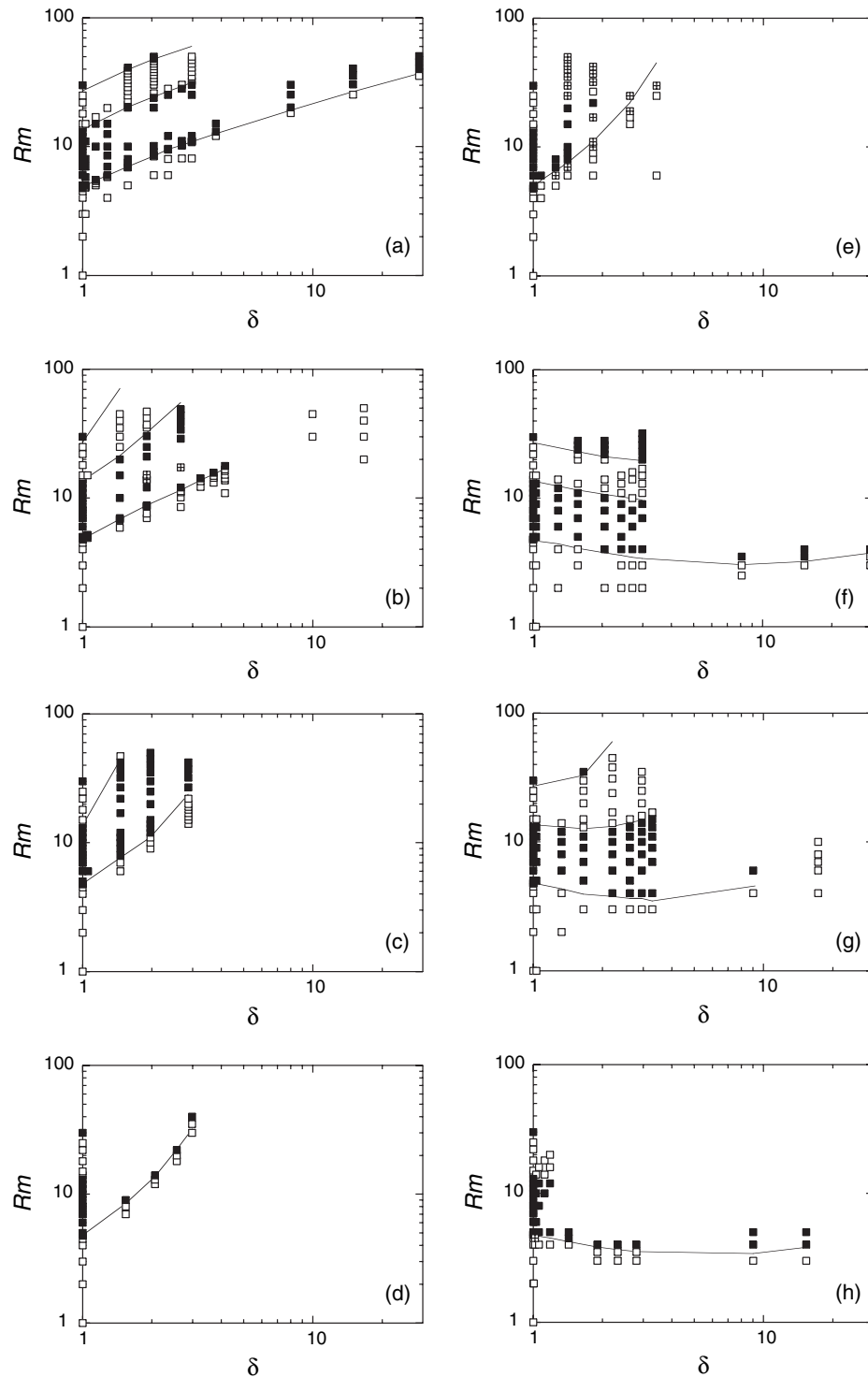


Figure 22. Parameter space for noise at $Re = 6$ for different noise parameters: (a) $\tau_c = 0$, $k_I = 1$; (b) $\tau_c = 0.03$, $k_I = 1$; (c) $\tau_c = 0.3$, $k_I = 1$; (d) $\tau_c = 2.7$, $k_I = 1$; (e) $\tau_c = 16.7$, $k_I = 1$; (f) $\tau_c = 0$, $k_I = 16$; (g) $\tau_c = 0.03$, $k_I = 16$; (h) $\tau_c = 0.3$, $k_I = 16$; (i) $\tau_c = 2.7$, $k_I = 16$; (j) $\tau_c = 16.7$, $k_I = 16$. \square : no-dynamo case; \boxtimes : undecided state; \blacksquare : dynamo case. The full lines are zero-Lyapunov exponent lines.

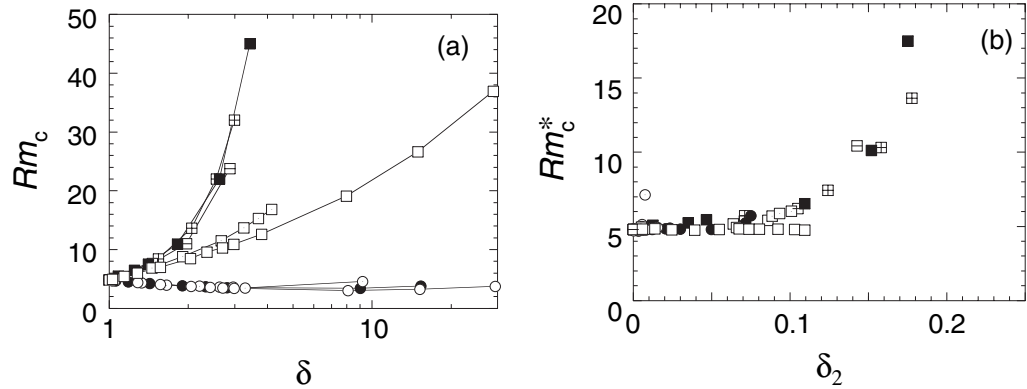


Figure 23. Evolution of the dynamo threshold for KS simulations with $\bar{u}(Re = 6)$. (a) Rm_c as a function of δ and (b) Rm_c^* as a function of δ_2 for different noise parameters: $k = 1$: \square $\tau_c = 0$; \boxplus $\tau_c = 0.03$; \boxtimes $\tau_c = 0.3$; \boxdot $\tau_c = 2.7$; \blacksquare $\tau_c = 16.7$; $k = 16$: \circ $\tau_c = 0$; \odot $\tau_c = 0.03$; \bullet $\tau_c = 16.7$.

(resp. decrease) the dynamo threshold. Furthermore, one sees that for small-scale noise, the decrease in the dynamo threshold is almost independent of the noise correlation time τ_c , while for the large scale noise, the increase is proportional to τ_c at small τ_c . At $\tau_c \gtrsim 0.3$, all curves $Rm_c(\delta)$ collapse onto the same curve. We have further investigated this behaviour to understand its origin. Increasing δ firstly increases the flow turbulent diffusivity $\eta_t = V_{rms} L_{int}$ with respect to its mean flow value, η_{MF} , computed using the energy and the integral length of the mean flow. Since the magnetic Reynolds number is essentially the ratio of the (mean or turbulent) flow diffusivity over the true diffusivity, this naturally produces an increase in the critical value. This effect can be corrected by considering the equivalent mean-field magnetic Reynolds number $Rm_c^* = Rm_c \eta_{MF} / \eta_t$. Secondly, an increase of δ produces an increase of the fluctuations of kinetic energy (see figure 20), quantified by $\delta_2 = \sqrt{\langle u^2 \rangle^2 - \langle u^2 \rangle^2} / \langle u^2 \rangle$. This last effect is more pronounced at $k_1 = 1$ than at $k_1 = 16$. It is amplified through increasing noise correlation time.

We thus re-analysed our data by plotting Rm_c^* as a function of δ_2 (figure 23(b)). All results tend to collapse onto a single curve, independently of the noise injection scale and correlation time. This curve tends to a constant equal to Rm_c^{MF} at low δ_2 . This means that the magnetic diffusivity needed to achieve dynamo action in the mean flow is not affected by spatial velocity fluctuations. This is achieved for small-scale noise, or large scale noise with small correlation time scale. In contrast, the curve diverges for δ_2 of the order of 0.2, meaning that time-fluctuations of the kinetic energy superseding 20% of the total energy annihilate the dynamo. In a real flow, or in the DNS, such fluctuations are more likely reached via non-stationary large scale, since they are the most energetic.

3.5.5. Comparison with theory. At small values of noise, $\delta \rightarrow 1$, one may compare our numerical results to an asymptotic theory by Fauve and Petrelis [33], linking the dynamo threshold to the noise amplitude $(\delta - 1)^{1/2}$.

Their prediction is that the correction to the dynamo threshold is zero at first-order $O((\delta - 1)^{1/2})$, and depends on the noise helicity at the next-order $O(\delta - 1)$. The correction is positive (resp. negative) if the noise helicity $\langle \mathbf{u} \cdot (\nabla \times \mathbf{u}) \rangle$ has same sign (resp. opposite sign) than the

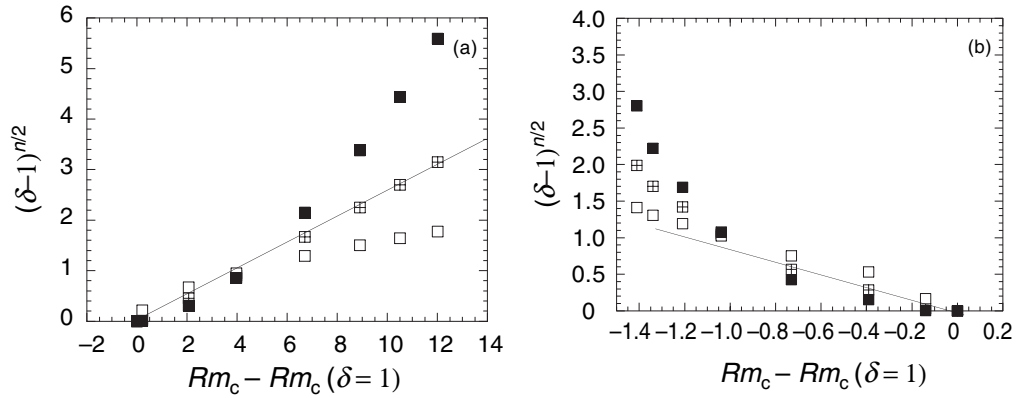


Figure 24. Evolution of different orders of noise amplitude $(\delta - 1)^{n/2}$ as a function of the correction to the dynamo threshold $Rm_c - Rm_c(\delta = 1)$ for KS simulations with $\bar{u}(Re = 6)$: (a) for a Markovian noise at $k_I = 1$ and $\tau_c = 0.03$ (b) for a Markovian noise at $k_I = 16$ and $\tau_c = 0$: $k = 1$: \square $n = 1$; \boxplus $n = 2$; \blacksquare $n = 3$.

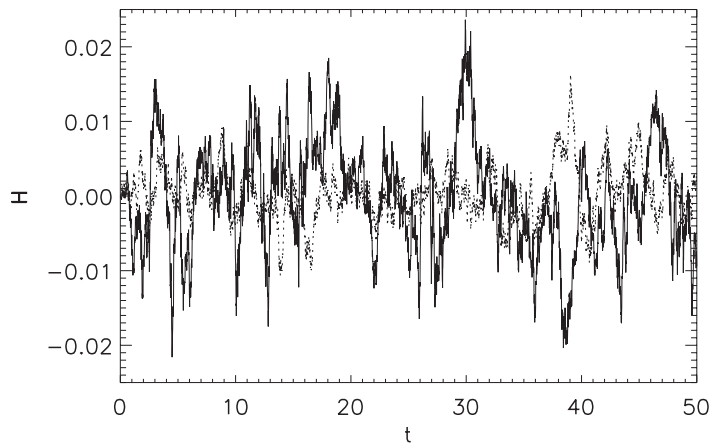


Figure 25. Helicity of a Markovian noise with $\tau_c = 0.03$ as a function of time: $-k_I = 1$; \cdots $k_I = 16$.

helicity of the basic flow. As a first check of this prediction, we therefore plotted $(\delta - 1)^{n/2}$ as a function of $Rm_c - Rm_c(\delta = 1)$ for $n = 1$ (first-order), $n = 2$ (second-order) and $n = 3$ (third-order), and looked for linear behaviour. Examples for large scale and small-scale noise are provided in figure 24). In all cases, we obtain the same kind of behaviour. One sees that indeed, the best linear behaviour until $\delta - 1 = 2$ is obtained for $n = 2$, indicating that the correction to threshold is at second-order in the noise amplitude. We have also tried to see if the sign of the correction depends on the helicity of the noise. This quantity strongly fluctuates in time. It is plotted in figure 25 for small and large scale Markovian noises with a correlation time of 0.3. The time average of the total helicity inside the box $[0; 2\pi]$ over the simulation time is very small -0.0001 for $k = 1$ and 0.0004 for the case $k = 16$. They are indeed of opposite signs, which could explain the sign of the correction we observe. However, we are not sure that such a small value is significant. Moreover, the helicity of the mean flow is 0, at variance with the

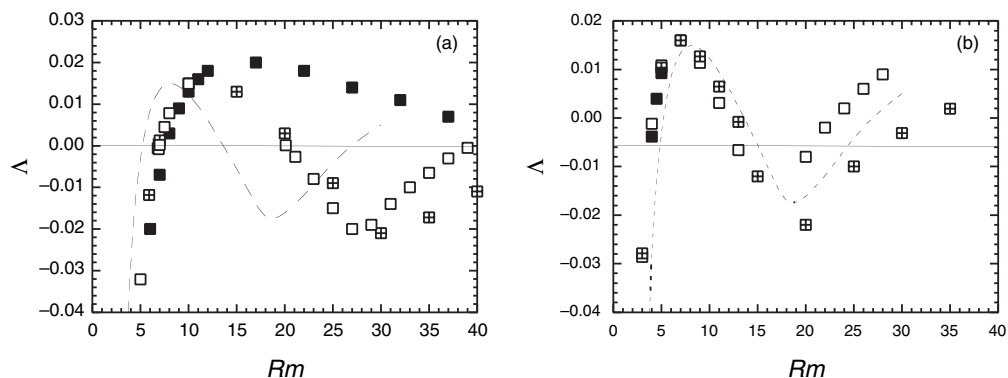


Figure 26. Evolution of the Lyapunov exponent versus Rm for different noise intensity and correlation time in KS simulations at $Re = 6$. The dotted line is the Lyapunov exponent at $\delta = 1$ (no noise): (a) for a Markovian noise at $k_I = 1$, $\delta = 1.5$ (b) for a Markovian noise at $k_I = 16$, $\delta = 1.7$: \square $\tau_c = 0$; \boxplus $\tau_c = 0.03$; \blacksquare $\tau_c = 0.3$.

Fauve–Petrelis theory, which requires a non-zero helicity of the mean flow. It therefore seems more likely that the corrections are due to the effects we mention above (mean energy and variance of the energy).

3.5.6. Lyapunov exponent. Another way to look at the influence of noise on the dynamo threshold is through the noise-induced deformation of the Lyapunov exponent. Figure 26 shows this deformation of the curve $\Lambda(Rm)$ for various values of δ , and different noise time correlation scales or injection scales. We have actually checked on our data (not shown) that the deformation of the Lyapunov exponent observed in the KS simulations is comparable to the deformation observed in DNS, at comparable noise intensity (i.e. δ) and for $\tau_c = 0.3$; $k_I = 1$. This reinforces the similitude between the DNS and a KS simulation at $\tau_c = 0.3$, $k_I = 1$.

3.5.7. Influence of mean flow. To check that our results are not affected by the choice of \bar{u} , we ran additional KS simulations with \bar{u} computed at $Re = 25, 46$ and 100 . Since the computational cost in these cases is much larger than in the case $Re = 6$, we focused on the case where the noise has a correlation time $\tau_c = 0.3$ or 2.7 and injection scale $k_I = 1$ for a few characteristic values of δ . Figure 27 shows that the dynamo threshold at various Re coincides with the dynamo thresholds of KS simulations at $Re = 6$, indicating that the influence of the mean flow on the dynamo threshold derived using the KS simulations is probably negligible.

3.5.8. Influence of spatial correlation: NS-I noise. The Markovian noise we used has no spatial correlation, at variance with real turbulence. Following [31], we therefore ran a few additional stochastic simulations using NS-noise computed as $\mathbf{v}' = A(\mathbf{u}(Re) - \bar{\mathbf{u}}(Re))$, where $\mathbf{u}(Re)$ is a velocity field computed in a DNS simulation at Reynolds Re , and A is an amplitude, tuned so as to get a desirable value for δ . The noise characteristic scale can be furthermore selected by appropriate filtering of \mathbf{v}' . Figure 28(a) shows the instantaneous kinetic energy of a large scale (keep all $k \leq 4$) or small scale (keep all $k > 8$) NS-noise at $Re = 25$, compared with the kinetic energy of a full DNS at $Re = 25$. One sees that the large-scale noise retains most of

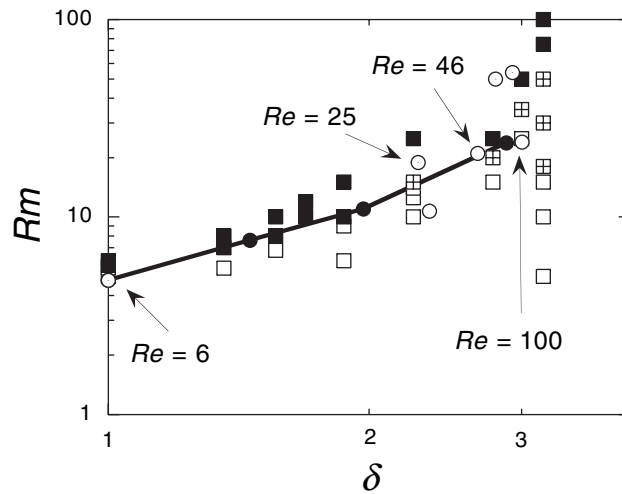


Figure 27. Evolution of the dynamo threshold as a function of δ for KS simulations with $k_I = 1$ using $\bar{u}(Re = 6)$, $\tau_c = 0.3$ (\bullet connected with lines), and \bar{u} at the Reynolds number corresponding to the DNS with equivalent δ (\circ for $\tau_c = 0.3$ and \odot for $\tau_c = 2.7$).

the kinetic energy, but involves slow time fluctuations, while the small-scale noise includes only a negligible part of the kinetic energy, but is responsible for most of the observable short time fluctuations of the DNS. When plugged into the stochastic simulations, these two types of noise lead to drastically different behaviour: the large-scale NS-noise increases the dynamo threshold with respect to the DNS, while the small-scale noise decreases substantially the dynamo threshold with respect to the DNS. For example, at $Re = 25$, the DNS gives $Rm_c = 14$, while the large-scale NS-noise with $\delta = 2.21$ gives $Rm_c = 18$, while a small-scale NS-noise with $\delta = 1.51$ (resp. $\delta = 2.19$) gives $Rm_c = 9$ (resp. $Rm_c = 11$). We have compared these values with the thresholds obtained for Markovian correlated noise in figure 28(b). The value for the large-scale NS-noise is larger than the asymptotic value obtained at the same δ in the Markovian large-scale noise when $\tau_c > 0.3$. The small-scale NS-noise has a lower threshold, that is above the value of the small-scale Markovian noise, but is comparable with the delta-correlated large-scale noise. In any case, the large-scale filtering applied to the NS-noise does indeed lead to thresholds that are substantially smaller than in the DNS. This reinforces the idea that it may be a good idea in real experiments to filter out the large-scale noise through an appropriate device.

3.6. Full coupled problem

Non-linear dynamos have also been studied, using simultaneous integrations of equation (2). Several interesting features have been found, at both linear and non-linear stages of the dynamo process. A summary of the DNS and LES we performed is provided in figure 29.

3.6.1. Linear stage: cycle between two states and oscillatory states for $Re < 10$. At a low kinetic Reynolds number, the basic flow is, as previously seen, characterized by several metastable states. The introduction of a seed magnetic field (of energy of the order of 10^{-3} of the kinetic energy) has a strong influence on the stability of the various states of the TG flow,

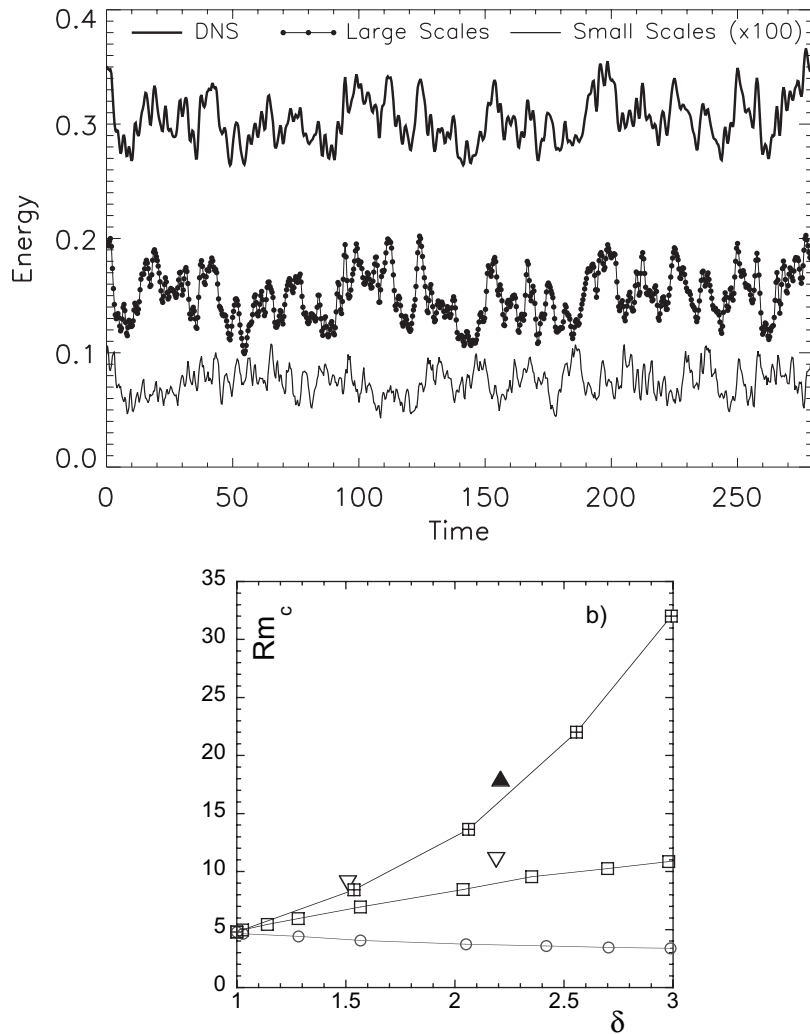


Figure 28. Stochastic simulations with NS-I noise: (a) instantaneous kinetic energy of a large-scale (keep all $k \leq 4$) or small-scale (keep all $k > 8$) NS-noise at $Re = 25$, compared with the kinetic energy of a full DNS at $Re = 25$. For better visibility, the energy of the small-scale noise has been multiplied by 100. (b) Evolution of the dynamo threshold (Rm_c as a function of δ) for KS–NS simulations with $\bar{u}(Re = 25)$ compared with KS simulations with Markovian noise, at different noise parameters: \blacktriangle KS simulations with large scale NS noise; ∇ : KS simulations with small-scale NS noise; KS simulations with Markovian noise at $k = 1$: \square $\tau_c = 0$; \boxplus $\tau_c = 2.7$; KS simulations with Markovian noise at $k = 16$: \circ $\tau_c = 0$.

even in the no dynamo regime. At low kinetic and magnetic Reynolds numbers ($Re, Rm < 10$), the magnetic field can temporarily stabilize the basic metastable state B, resulting in cycles in between the state B and the state M. The velocity field then oscillates in between the two states, and the magnetic field growth is made of portions of exponential growth or decays, corresponding to growth rates of the two different states (figure 30).

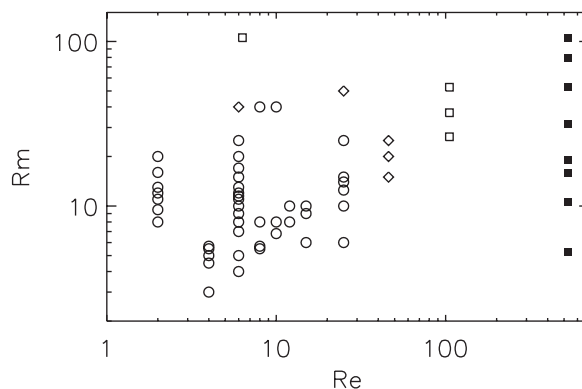


Figure 29. Parameters of the DNS (open symbols) and LES (filled symbols) of full coupled system equation (2). The three symbols represent three different spatial resolutions: 64^3 (\circ), 96^3 (\diamond) and 128^3 (\square).

Increasing further the magnetic Reynolds number $Rm > 20$, one observes the appearance of complex Lyapunov exponents, with magnetic energy made of a combination of exponential growth and oscillation (figure 31) in the magnetic energy, accompanied by oscillation in the kinetic energy. The location of apparition of these oscillatory modes roughly corresponds to the end of the first dynamo window in the kinematic case.

3.6.2. Linear stage: noise versus magnetic field. Around $Re = 15$, the magnetic field allows exploration of all the various metastable states, resulting in short periods of exponential growth, followed by random wandering as the system searches for the largest eigen-component of the instantaneous state visited. The total Lyapunov exponent is then less than any Lyapunov exponent of any metastable state present in the system. An example is provided in figure 32. This weakening of the Lyapunov exponent due to the noisy nature of the velocity field is reminiscent of the disorientation effect predicted by Leprovost and Dubrulle [29] in their stochastic model of dynamo.

For larger values of $Re > 15$, the magnetic field plays the role of a noise, allowing direct transition of the velocity field towards the turbulent state, even in the absence of the dynamo effect. Looking at the spectra, we observed that even a small magnetic field favors the building of a $k = 1$ component in the kinetic energy spectra (figure 33), in a way similar to an external noise. Note that a similar population of the low frequency spectrum has been observed in the time spectra of a VK flow, during the transition from chaos to turbulence [34].

At the end of a no-dynamo MHD simulation with an asymptotically vanishing magnetic field, one then obtains a velocity field different than the velocity field obtained by integration of the hydrodynamic equation (1) with the same initial condition but no noise, as if the magnetic field had vaccinated the flow. This special feature has been recognized a few years ago by [11], who gave it this name.

3.6.3. Linear stage: critical dynamic magnetic Reynolds number. In all the simulations, the Lyapunov exponent strongly fluctuates with time. We have therefore used a finite-time average of this quantity to compute the dynamo threshold by the condition $\overline{\Lambda}(Rm_c^{\text{turb}}) = 0$. The various critical magnetic Reynolds numbers we obtained in this case are reported in figure 34 and

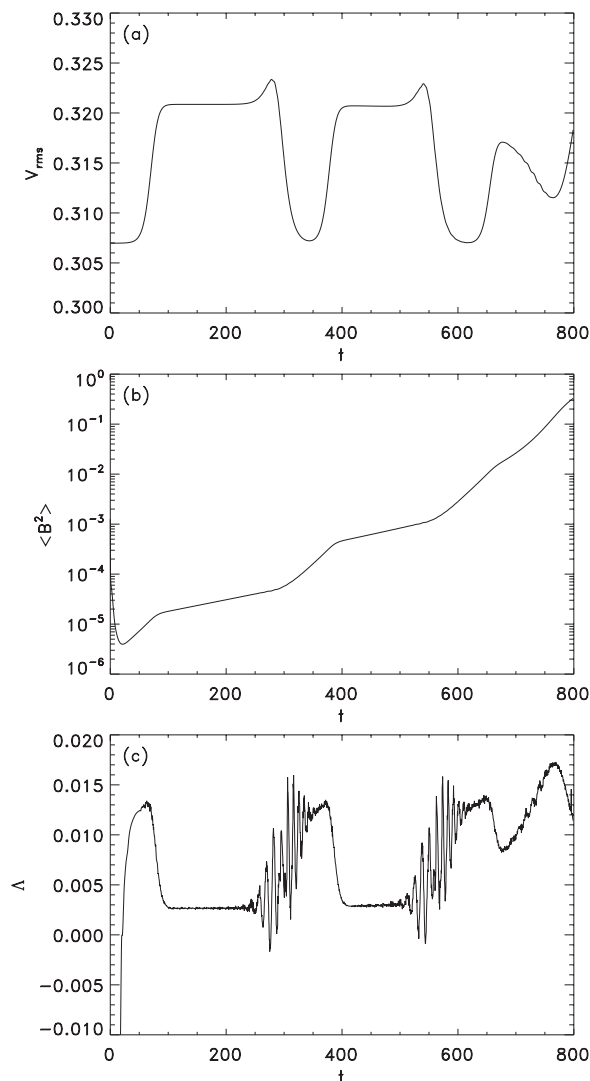


Figure 30. Example of a cycle between state B and state M at $Re = Rm = 6$. (a) V_{rms} as a function of time; (b) magnetic energy as a function of time; (c) Lyapunov exponent as a function of time.

table 3. One can see that they are very much larger than the values obtained in the kinematic case. An explanation of this effect could be that the turbulence is akin to a noise, with a specific correlation time and characteristic scale [35]. Indeed, it can be shown in figure 27 that the dynamo threshold obtained in the DNS coincides with the dynamo thresholds of KS simulations at $Re = 6$ obtained for large-scale noise with correlation time $\tau_c = 0.3$. Note that another interpretation is proposed by [3] in the present issue.

3.6.4. Link with the negative eddy-diffusivity. One may also notice that below $Re = 3$, no dynamo is observed. This is reminiscent of the critical Reynolds number for presence of a large-scale negative eddy-diffusivity instability computed by Lanotte *et al* [22], indicating that this mechanism could be at work, at least at a low Reynolds number. A partial confirmation

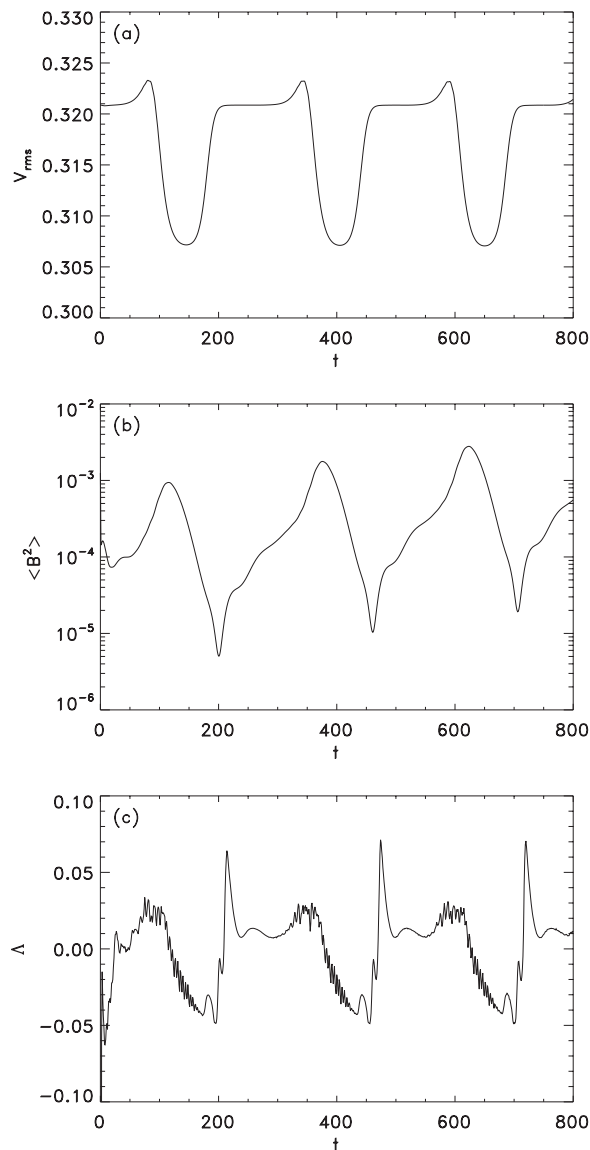


Figure 31. Example of an oscillatory growth at $Re = 6$, $Rm = 25$. (a) V_{rms} as a function of time; (b) magnetic energy as a function of time; (c) Lyapunov exponent as a function of time.

of this suspicion can be obtained by looking at the structure of the neutral mode, and see whether it has the planar structure characteristic of the negative-eddy-diffusivity. This has been done by Ponty *et al* [4] who indeed observe a planar structure for the dynamo mode in the first window of instability, suggestive of the negative-eddy-viscosity instability. Note that this instability seems to be forbidden in a symmetric TG code since such spatial structure is forbidden because of overall rotational invariance. One is then potentially left only with the second dynamo mechanism (corresponding to the second window of dynamo action), resulting in larger dynamo threshold. This therefore explains previous results of Nore *et al* [19], who noticed that the critical magnetic Reynolds number for symmetric simulations are larger than in a non-symmetric case, but can be substantially decreased by using forcing at larger

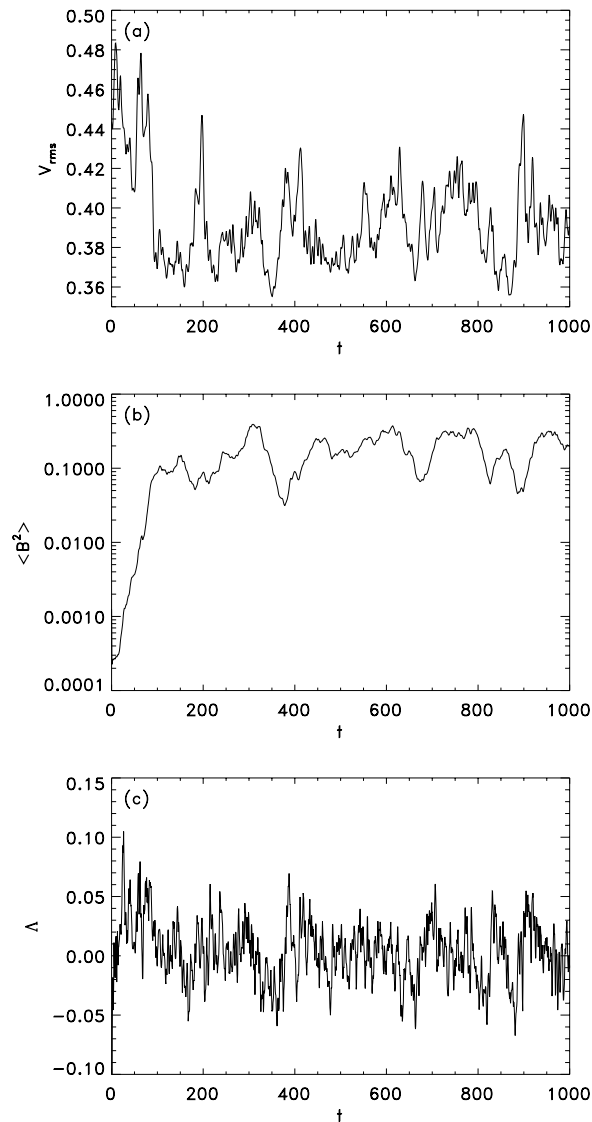


Figure 32. Example of nonlinear dynamo $Re = 15$ and $Rm = 50$. (a) V_{rms} as a function of time; (b) magnetic energy as a function of time; (c) Lyapunov exponent as a function of time.

wavenumber: from $Rm_c = 144$ at $k_0 = \sqrt{3}$, up to $Rm_c = 11$ at $k_0 = 12$. They noticed that the increase of the forcing wavenumber could favor the apparition of large-scale instabilities, presumably the negative-eddy-viscosity instability.

3.6.5. Non-linear stage: intermittent versus mean field dynamo. After the initial exponential growth, the magnetic field becomes large enough to react back on the velocity field through the Lorentz force, initializing a nonlinear saturation. We have observed two main types of saturation: intermittent dynamo and mean field dynamo (see figure 35). In the first case, the magnetic field behavior is very intermittent, made of bursts of magnetic activity followed by (relatively) long lasting periods of inactivity (see figure 36). In this case, the probability

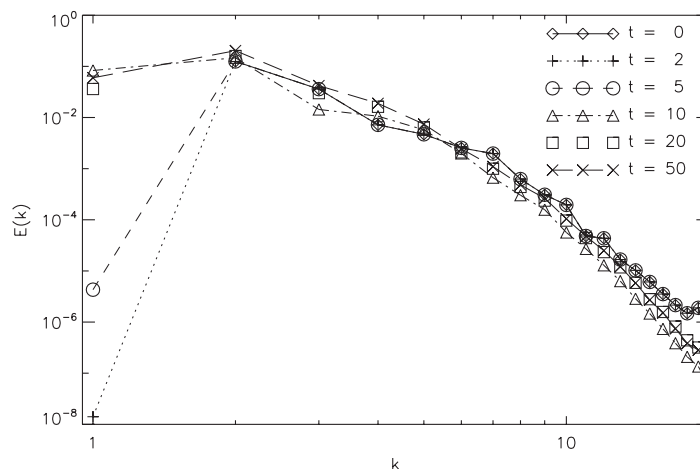


Figure 33. Evolution of the kinetic energy spectrum, at $Re = 25$, $Rm = 6$ (no dynamo case), as a function of time. One sees the building of a strong $k = 1$ component, in a similar way to the noisy case.

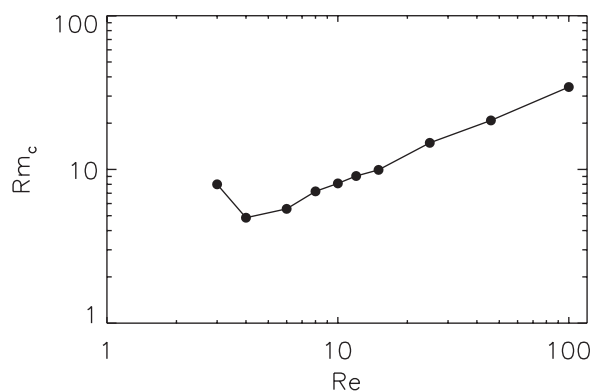


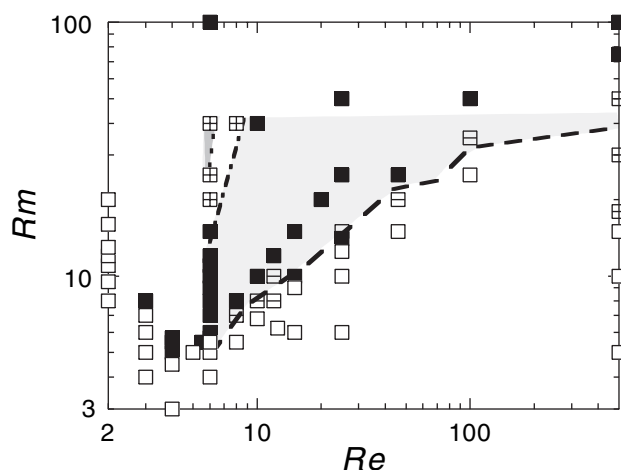
Figure 34. Critical magnetic Reynolds number as a function of the Reynolds number.

distribution of magnetic energy is sharply peaked towards the origin: the most probable value is zero (see figure 36). This type of dynamo is reminiscent of the intermittent dynamo proposed by Leprovost and Dubrulle [29]. In our case, the intermittent dynamo was clearly identified only in the low Re , large Rm regime, in the parameter range corresponding to the transition between the two dynamo windows for the mean field. More precisely, the parameter range for an intermittent dynamo seems to coincide with the no-dynamo window of the mean field, distorted by noise (see figure 35), reinforcing the analogy between DNS–MHD simulations and KS simulations with Markovian noise. We do not exclude the possibility of an intermittent dynamo near the onset of the dynamo action at larger Re (typically for $Re \geq 30$, corresponding to our undecided state), but their study and confirmation would involve computation time beyond our capacity.

Note that the intermittent dynamos we observe are seemingly quite different from the previously reported intermittent dynamo (see e.g. [36]). In these cases, the dynamo was observed to be spatially intermittent, in the sense that the magnetic field structures were irregularly disposed over the space. The magnetic energy, however, fluctuates around a mean value. In our case,

Table 3. Critical dynamical magnetic Reynolds number for various Reynolds numbers.

Re	Rm_c	V_{rms}
3		0.31
4	4.85	0.31
6	5.54	0.32
8	7.20	0.35
10	8.11	0.38
12	9.06	0.39
15	9.93	0.41
25	14.89	0.45
46	20.83	0.50
100	34.36	0.52

**Figure 35.** Simulations parameter space. Squares refer to DNS-MHD and LES-MHD simulations, and shaded areas to windows of dynamo action for kinematic-stochastic simulations at $Re = 6$ with $k_1 = 1$, $\tau_c \geq 0.3$. Note the tiny dynamo window near $Re = 6$, $Rm = 40$. \square : no-dynamo case; \boxplus : intermittent dynamo; \blacksquare : dynamo case; \boxdot : undecided state; — Rm_c^{turb} ; -- Rm_c^{MF} ; - · - · end of the first dynamo window; ··· beginning of the second dynamo window.

the dynamics of the magnetic fields proceeds through bursts in time, meaning that there is actually a large probability that there is no magnetic field at all anywhere in the box. This strange behaviour is related to on-off dynamics (typical of systems with multiplicative noise [29]) and has been reported before in a truncated simulation of an ABC flow [37], near the dynamo threshold, or, more recently, in an experimental Bullar-VK dynamo [32], or in the VKS2 experiment [6].

Dynamos with a non vanishing mean field were observed most of the time. They are characterized by a saturation occurring around a well-defined mean value. At low Reynolds numbers (typically Re and $Rm < 15$), the saturation is stationary and evolves towards a

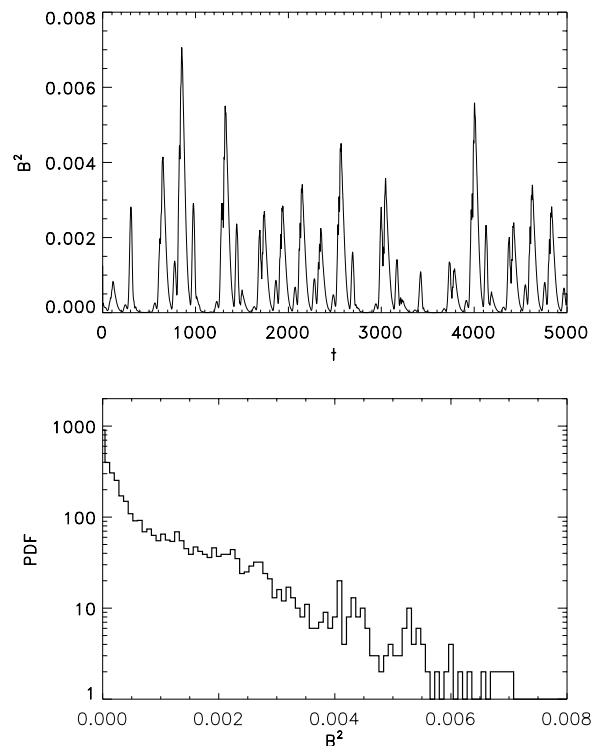


Figure 36. Example of intermittent dynamo at $Re = 6$, $Rm = 40$. (a) Magnetic energy as a function of time; (b) PDF of the magnetic energy.

turbulent state for large Reynolds numbers (see figure 37). In that case, the probability distribution is distributed around the mean value, and decreases towards zero or infinity (see figure 37).

3.6.6. Nonlinear stage: a bifurcation sequence at low Re . We have followed a bifurcation sequence at $Re = 6$, and $4 < Rm < 100$ and found that the transition to turbulence occurs via successive bifurcations (figure 38) reminiscent to what is observed in systems with low degrees of freedom: the stationary dynamo excited nonlinearly at $Rm = 5.78$ bifurcates into an oscillatory state at $Rm \sim 7$ until $Rm = 12$ where cycles between the unstable ground state and an unstable upper dynamo state begin to appear. These cycles are observed until the beginning of the second dynamo window $Rm \sim 25$ where a second sequence of bifurcations begins. The resulting dynamos are oscillatory, switching towards irregular (intermittent) dynamos around $Rm \sim 40$. At $Rm = 100$, the dynamo is turbulent, with a well defined mean value. This sequence of bifurcations is reminiscent of what has been previously observed in periodic simulations of the ABC flow [38]. Oscillations in low Reynolds number TG flow have also been reported by Mininni *et al* in [39]. They noted that as the Reynolds number is increased, the oscillations disappear and the energies become more stationary. However, they were able to detect some vestige of the periodic behaviour in the magnetic energy. It is therefore likely that the sequence of bifurcations we observe at a low Reynolds number disappears at a higher Reynolds number due to fluctuations.

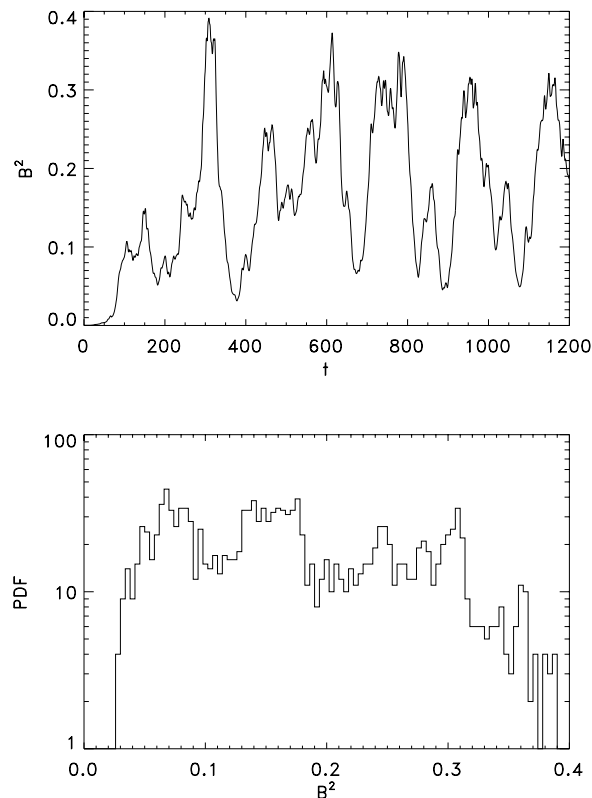


Figure 37. Example of a dynamo with a mean-field at $Re = 25$, $Rm = 50$. (a) Magnetic energy as a function of time; (b) PDF of the magnetic energy.

4. Discussion

The present study of the TG flow reveals several distinguished features that are worth summarizing: (i) a complex parameter space, with coexistence of several metastable states and possible transitions in between them, that may be mediated by a magnetic field; (ii) the existence of two windows of dynamo instability; (iii) the increase of the dynamo threshold with respect to the kinematic dynamo threshold for increasing the Reynolds number that bears strong similarities with the increase observed in the presence of large-scale noise with increasing kinetic energy; (iv) the existence of different regimes of dynamo saturation, and a sequence of bifurcations in between these regimes that is reminiscent of systems with a few degrees of freedom.

An interesting open question is therefore whether these features are of any relevance to the VKS experiments, that are operated in a range of parameters quite different from our numerical simulations, with a kinematic Reynolds number about 10^4 larger than ours. Regarding the complex parameter space, there is indeed indication that such high Reynolds number VK flow without a magnetic field is characterized by different metastable states, with different symmetry properties [34]. Whether a magnetic field can influence the transition in between these states is currently a question explored in the VKS experiment. The influence of the large-scale noise on the dynamo action is also a question that can be addressed in future VKS experiments, thanks to devices monitoring large-scale vortices that are presently tested and implemented. For example, with stainless propellers, no dynamo action has yet been achieved, but it has been noted that the

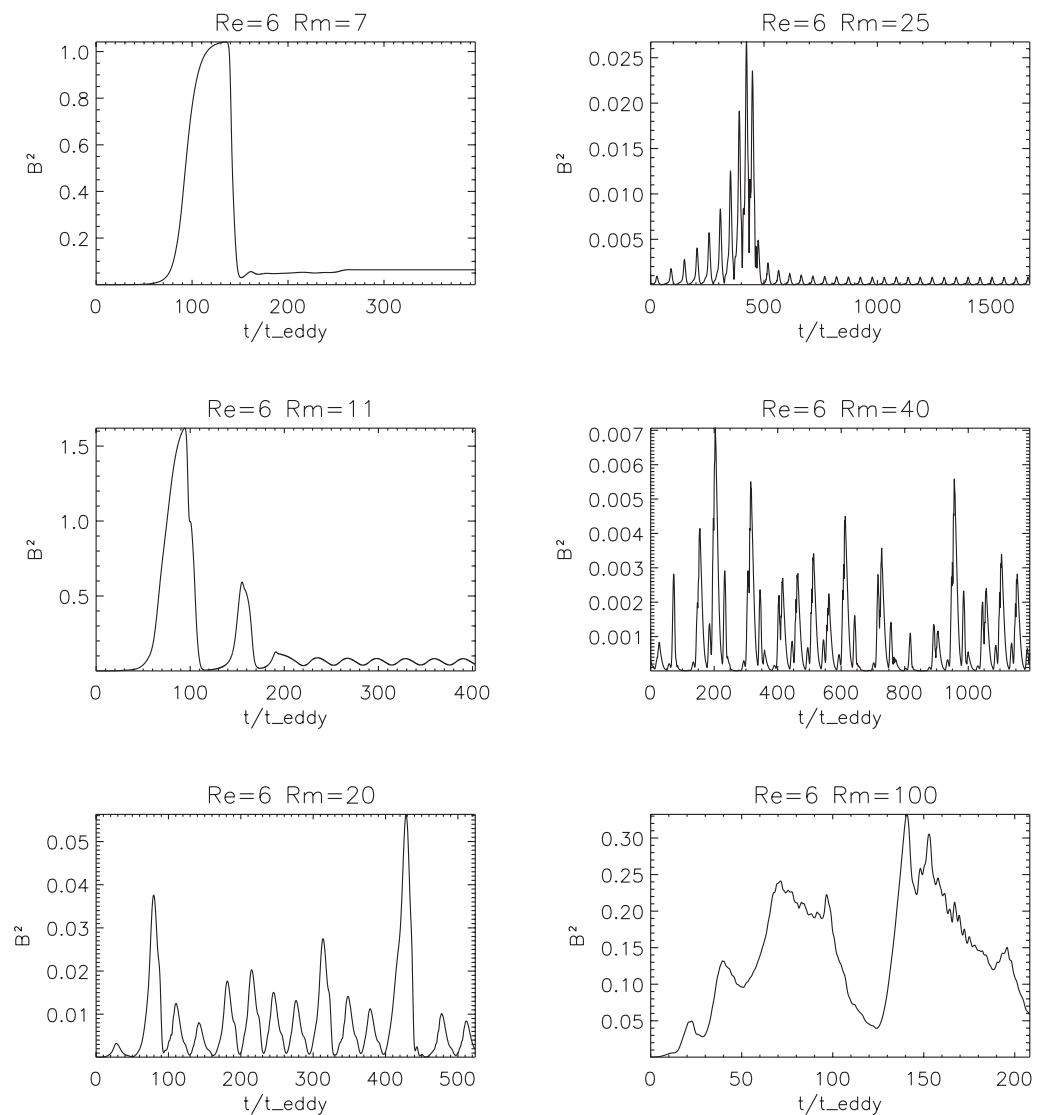


Figure 38. Sequence of bifurcations observed at $Re = 6$ for increasing Rm . Note the transient unstable high-dynamo mode occurring after the linear growth at low Rm before saturation of the dynamo towards a lower amplitude. This second dynamo mode is stationary at $Rm = 7$, oscillatory at $Rm = 11$, chaotic at $Rm = 20$. Starting around $Rm = 25$, new dynamo modes are seen, after a sequence of oscillatory growth towards a second unstable high dynamo mode. These modes are oscillatory for $Rm = 25$, intermittent for $Rm = 40$ and turbulent for $Rm = 100$.

addition of an annulus at the mid-plane (so as to stabilize large-scale vortices) strongly increases the induction [40]. In the configuration with iron propellers and the annulus at the mid-plane, dynamo action has been observed [8] at magnetic Reynolds numbers slightly below critical magnetic Reynolds numbers computed in kinematic codes for stainless propellers [24, 41, 42]. An interesting open question is whether the dynamo threshold will change if the annulus is removed, and large-scale motions of the mixing layer are permitted. Finally, different regimes of dynamo saturation have indeed been observed in the VKS experiment, with dynamics similar

to systems with few degrees of freedom [6]. These regimes are mostly observed in situations where a mean rotation is superimposed to the flow. Since one of the influences of the rotation is to damp velocity fluctuations, one may wonder whether the complex dynamos with the rotation of VKS are related to the sequence of bifurcations we observe in TG flow at low Reynolds number, with few fluctuations.

This confirms the interest of the TG flow as a prototype to understand, at least qualitatively, some results of VKS experiments as first suggested in [5].

Acknowledgments

We thank C Nore for many interesting discussions and comments, and Y Ponty and J-F Pinton for ongoing collaboration, exchanges and discussion on the TG flow. This work benefited from computer time allocated by IDRIS run by French CNRS and by CRIHAN (Centre de Ressource en Informatique de Haute Normandie, France). We thank the ‘Programme National de Planétologie’, the GDR Turbulence and the GDR Dynamo for support. We have benefited from numerous discussions with our colleagues from GIT and from Lille University.

References

- [1] Brachet M E, Meiron D I, Orszag S A, Nickel G G, Morf R H and Frisch U 1983 Small-scale structure of the Taylor-Green vortex *J. Fluid. Mech.* **130** 411
- [2] Nore C, Brachet M E, Politano H and Pouquet A 1997 Dynamo action in the Taylor–Green vortex near threshold *Phys. Plasma* **4** 1–3
- [3] Ponty Y, Mininni P D, Montgomery D, Pinton J F, Politano H and Pouquet A 2007 *New J. Phys.* **9** 296
- [4] Ponty Y, Mininni P D, Pinton J F, Politano H and Pouquet A 2005 Numerical study of dynamo action at low magnetic Prandtl numbers *Phys. Rev. Lett.* **94** 164502
- [5] Ponty Y, Politano H and Pinton J F 2004 Simulation of the induction at low magnetic Prandtl number *Phys. Rev. Lett.* **92** 144503
- [6] Berhanu M 2007 Magnetic field reversals in an experimental turbulent dynamo *Europhys. Lett.* **77** 59001
- [7] Bourgoin M *et al* 2002 Magnetohydrodynamics measurements in the von Karman sodium experiment *Phys. Fluids* **14** 3046
- [8] Monchaux R *et al* 2007 Generation of a magnetic field by dynamo action in a turbulent flow of liquid sodium *Phys. Rev. Lett.* **98** 044502
- [9] Petrelis F, Bourgoin M, Marie L, Burgete J, Chiffaudel A, Daviaud F, Fauve S, Odier P and Pinton J F 2003 Nonlinear magnetic induction by helical motion in a liquid sodium turbulent flow *Phys. Rev. Lett.* **90** 174501
- [10] Volk R *et al* 2006 Transport of magnetic field by a turbulent flow of liquid sodium *Phys. Rev. Lett.* **97** 074501
- [11] Nore C and Brachet M E 2006 private communication
- [12] Lifschitz A 1994 On the instability of certain motions of an ideal incompressible fluid *Adv. Appl. Math.* **15** 404–36
- [13] Lifschitz A and Hameiri E 1991 Local stability conditions in fluid-dynamics *Commun. Pure. Appl. Math.* **46** 1379–408
- [14] Sipp D and Jacquin L 1998 Elliptic instability of 2D flattened Taylor-Green vortices *Phys. Fluids* **10** 839–49
- [15] Leblanc S and Godeferd F S 1999 An illustration of the link between ribs and hyperbolic instability *Phys. Fluids* **11** 497–9
- [16] Lundgren T S and Mansour N N 1996 Transition to turbulence in an elliptic vortex *J. Fluid Mech.* **307** 43–62
- [17] Basdevant C, Legras B and Sadourny R 1981 A study of barotropic model flows: Intermittency, waves and predictability *J. Atmos. Sci.* **38** 2305

- [18] Chollet J P and Lesieur M 1981 Parametrization of small-scales of 3-dimensional isotropic turbulence utilizing spectral closures *J. Atmos. Sci.* **38** 2747
- [19] Nore C, Brachet M E, Politano H and Pouquet A 2001 *Dynamo and Dynamics, a Mathematical Challenge, Cargese, 21–26 August 2000* ed P Chossat *et al* (Dordrecht: Kluwer) pp 1–3
- [20] Nore C, Tuckerman L S, Daube O and Xin S 2003 The 1:2 mode interaction in exactly counter-rotating von Karman swirling flow *J. Fluid. Mech.* **477** 51
- [21] Nore C, Moisy F and Quartier L 2005 Experimental observation of near-heteroclinic cycles in the von Kàrmàn swirling flow *Phys. Fluids* **17** 064103
- [22] Lanotte A, Noullez A, Vergassola M and Wirth A 1999 Large-scale dynamo produced by negative magnetic eddy diffusivities *Geophys. Astrophys. Fluid Dyn.* **91** 131–46
- [23] Marié L, Normand C and Daviaud F 2006 Galerkin analysis of kinematic dynamos in the von Karman geometry *Phys. Fluids* **18** 017102
- [24] Ravelet F, Chiffaudel A, Daviaud F and Léorat J 2005 Toward an experimental von Kármán dynamo: Numerical studies for an optimized design *Phys. Fluids* **17** 117104
- [25] Arnold V I and Korkina E 1983 The growth of magnetic-field in a 3-dimensional steady incompressible flow *Vest. Mosk. Un. Ta. Ser. I Matem. Mekh.* **3** 43
- [26] Galloway D J and Frisch U 1996 Dynamo action in a family of flows with chaotic streamlines *Geophys. Astrophys. Fluid Dyn.* **36** 53
- [27] Lau Y T and Finn J M 1993 Fast dynamos with finite resistivity in steady flows with stagnation points *Phys. Fluids B* **5** 365
- [28] Ponty Y 2006 private communication
- [29] Leprovost N and Dubrulle B 2005 The turbulent dynamo as an instability in a noisy medium *Eur. Phys. J. B* **44** 395
- [30] Mallick K and Marcq P 2004 Noise-induced reentrant transition of the stochastic Duffing oscillator *Eur. Phys. J. B* **38** 99
- [31] Leprovost N, Dubrulle B and Plunian F 2006 *Magnetohydrodynamics* **42** 131
- [32] Bourgoin M, Volk R, Plihon N, Augier P, Odier P and Pinton J F 2006 An experimental Bullard-von Karman dynamo *New J. Phys.* **8** 329
- [33] Pétrélis F and Fauve S 2001 Saturation of the magnetic field above the dynamo threshold *Eur. Phys. J. B* **22** 273
- [34] Ravelet F, Chiffaudel A and Daviaud F 2007 *Phys. Fluids* submitted
- [35] Laval J P, Blaineau P, Leprovost L, Dubrulle B and Daviaud F 2006 Influence of turbulence on the dynamo threshold *Phys. Rev. Lett.* **96** 204503
- [36] Meneguzzi M, Frisch U and Pouquet A 1981 Helical and Nonhelical Turbulent Dynamos *Phys. Rev. Lett.* **47** 1060
- [37] Sweet D, Ott E, Finn J M, Antonsen T M and Lathrop D P 2001 Blowout bifurcations and the onset of magnetic activity in turbulent dynamos *Phys. Plasmas* **8** 1944
- [38] Podvigina O M 2003 A route to magnetic field reversals: An example of an ABC-forced nonlinear dynamo *Geophys. Astrophys. Fluid Dyn.* **97** 149
- [39] Mininni P, Ponty Y, Montgomery D, Pinton J-F, Politano H and Pouquet A 2005 Non-linear behaviour of a non-helical dynamo *Astrophys. J.* **626** 853
- [40] Ravelet F *et al* 2007 Magnetic induction in a turbulent flow of liquid sodium: mean behaviour and slow fluctuations *Phys. Fluids* submitted
- [41] Laguerre R, Nore C, Léorat J and Guermond J L 2006 Effects of conductivity jumps in the envelope of a kinematic dynamo flow *C. R. Mécanique* **334** 593–8
- [42] Stefani F, Xu M, Gerbeth G, Ravelet F, Chiffaudel A, Daviaud F and Léorat J 2006 Ambivalent effects of added layers on steady kinematic dynamos in cylindrical geometry: application to the VKS experiment *Eur. J. Mech. B* **25** 894–908